MT-CWR-089-038

(4)

ANNUAL REPORT

Investigations Into the Infiltration Kinetic Wettabi ty
and Interfacial Bond Strength of Al/SiC mposit

Submitted to:
Dr. Steven Fishman
Office of Naval Research
Arlington, Virginia 22217

Submitted by:
Glen R. Edwards and David L. Olsc n
Center for Welding and Joinin; Research
Colorado School of Mi es
Golden, Colorado 804(1

DTIC
ELECTE
AUG 16 1989
D

July, 1989

CENTER FOR WELDING RESEARCH
Colorado School of Mines
Golden, Colorado 80401

CSM

TABLE OF CONTENTS

PROJECT SUMMARY

Research accomplishments on this project during the research period 88-89 are in three distinct areas: infiltration kinetics, wettability studies, and predictions of interfacial properties. These areas will be presented in three separate sections.

Section 1 - Infiltration Kinetics:

Infiltration studies were based on the porous compact experiments. Our earlier research efforts (1,2) have established the existence of an incubation time before any infiltration can be initiated. A pre-conditioning reaction model was hypothesized to explain the incubation time. The rate equation for pre-conditioning was experimentally established. Also, a threshold pressure, the minimum pressure required for infiltration after incubation, was estimated.

Section 2 - Wettability Studies:

Wettability studies are based on surface tension measurements from the capillary rise experiment. A theoretical analysis was made to correlate the observed variation in interfacial tension from alloying additions. The oxide layers on the ceramic and the molten metal were found to have a strong influence on the wetting behavior at the interface.

Section 3 - Predictions of Interfacial Properties:

A novel theoretical model that predicts the interfacial properties prior to fabrication was developed. A key aspect of this approach was the incorporation of an established optical technique to determine the surface properties of a solid. Calculated interfacial bond energies of pure metals, Cu-Zn alloys, and Al-SiC interfaces are presented.

The results from all these experiments are simultaneously being sent for publication.

1.0 INFILTRATION KINETICS

1.1 Background

The theoretical model and the experimental setup used for porous

compact studies are described in the previous reports (1,2). In this

phase of the study, unsintered compacts of ~40μm-diam. α-SiC $>$ *Silicon carbide*

particles were infiltrated with pure aluminum. The infiltration distance,

the distance to which the liquid metal penetrates the porous compact, was

measured as a function of time for different temperatures and pressures.

The results are plotted as infiltration distance versus $(time)^{1/2}$ (Figs.

1.1-1.5) in accordance with a theoretical analysis previously reported.,

(3). (A least square analysis was carried out to fit a straight line

through the data points.)

1.2 Discussion

1.2.1 Incubation Studies

The minimum time required for the initiation of infiltration, termed

here the incubation time, can be estimated from data such as those shown

in Figs. 1.1-1.5 by extrapolating the line to zero infiltration distance.

The physical significance of the incubation time has been previously

explained to be associated with pre-conditioning the infiltration front by

means of vapor condensation (2).

At a constant pressure, the inverse of incubation time (rate of

pre-conditioning) was found to depend exponentially on temperature of

infiltration. This is indicative of an activation controlled rate

mechanism.

Figure 1.1 Infiltration distance versus (time)$^{1/2}$ for aluminum in SiC at 15 psi (103 kPa).

Figure 1.2 Infiltration distance versus (time)$^{1/2}$ for aluminum in SiC at 25 psi (172 kPa).

Figure 1.3 Infiltration distance versus (time)$^{1/2}$ for aluminum in SiC at 30 psi (207 kPa).
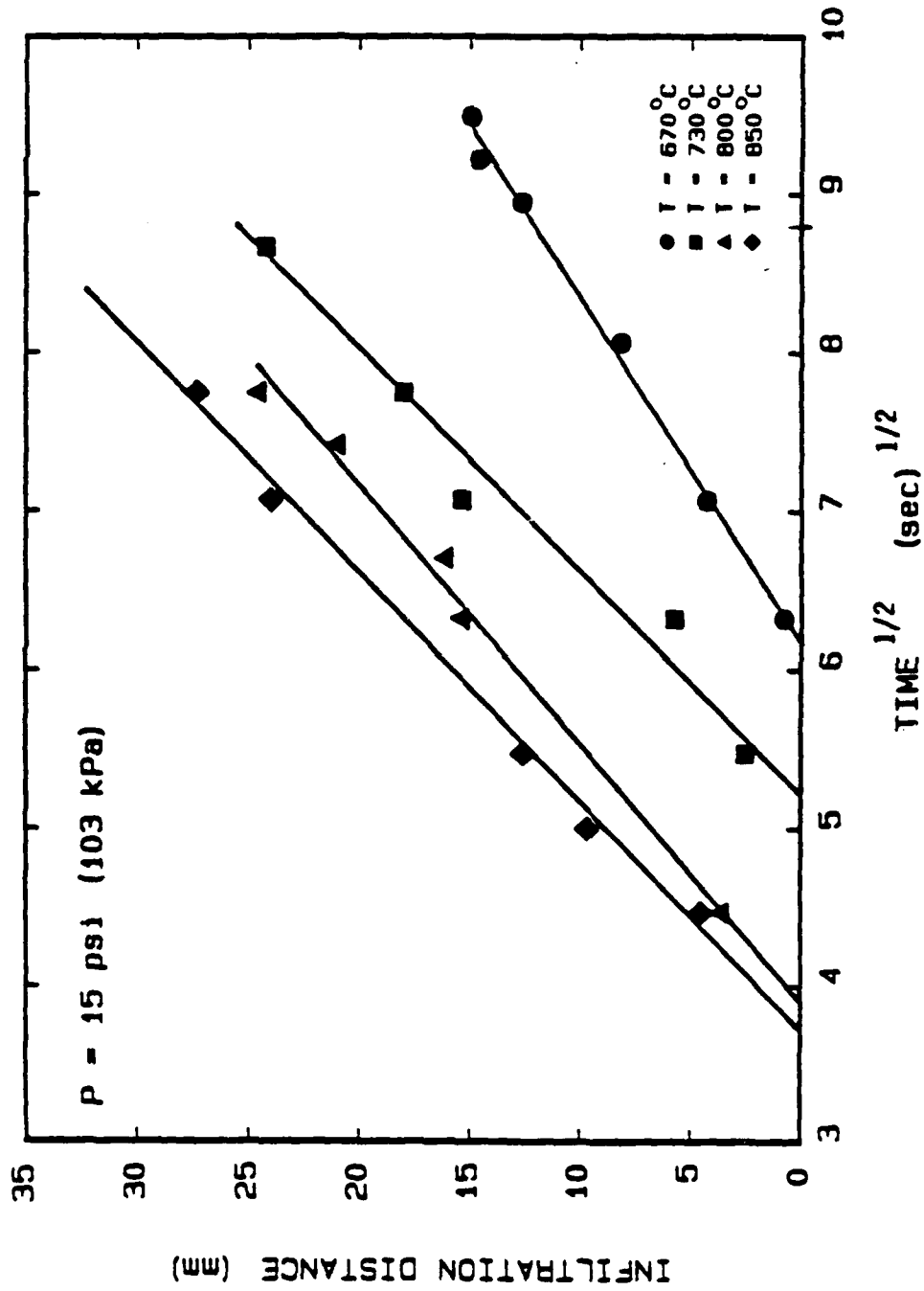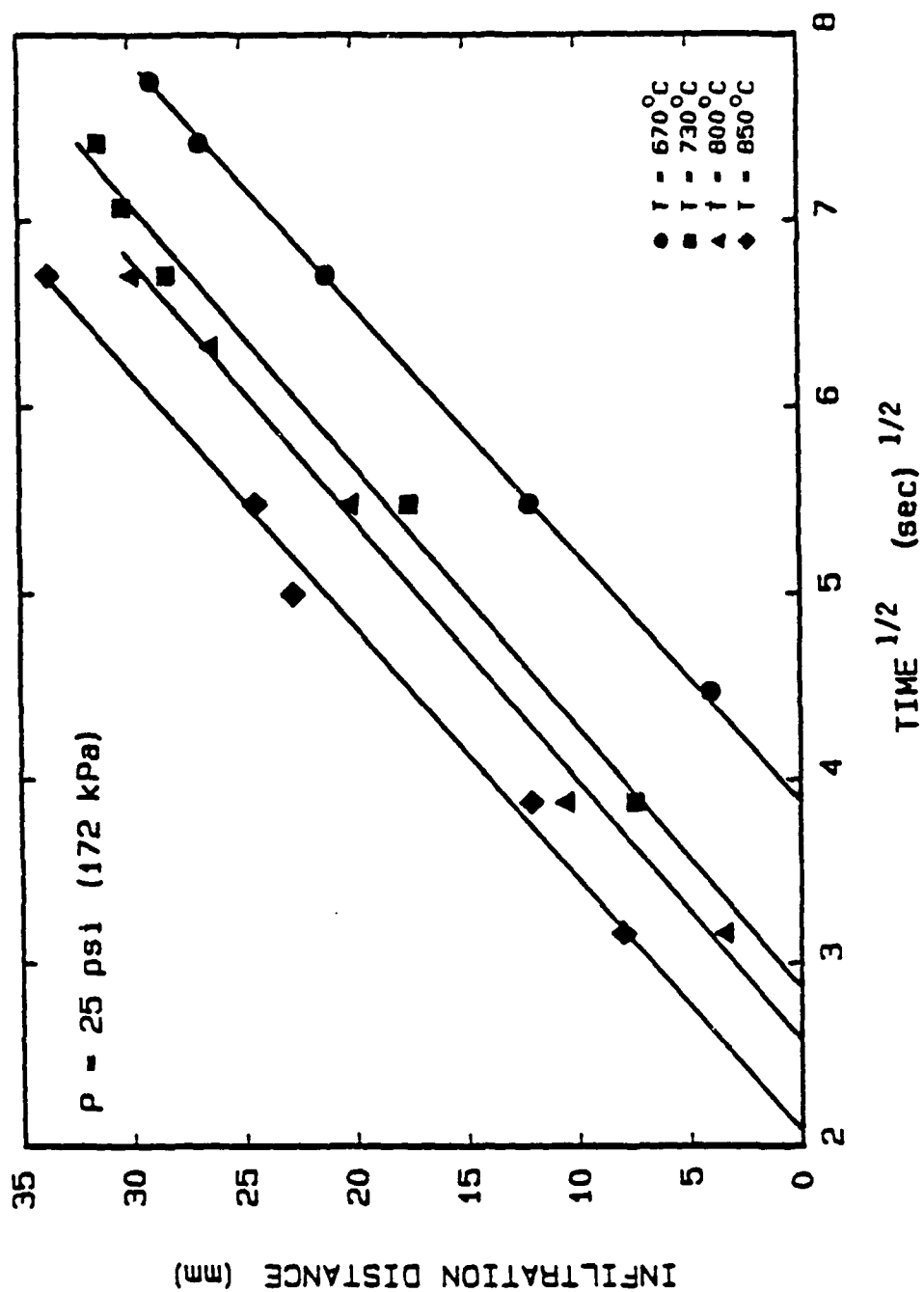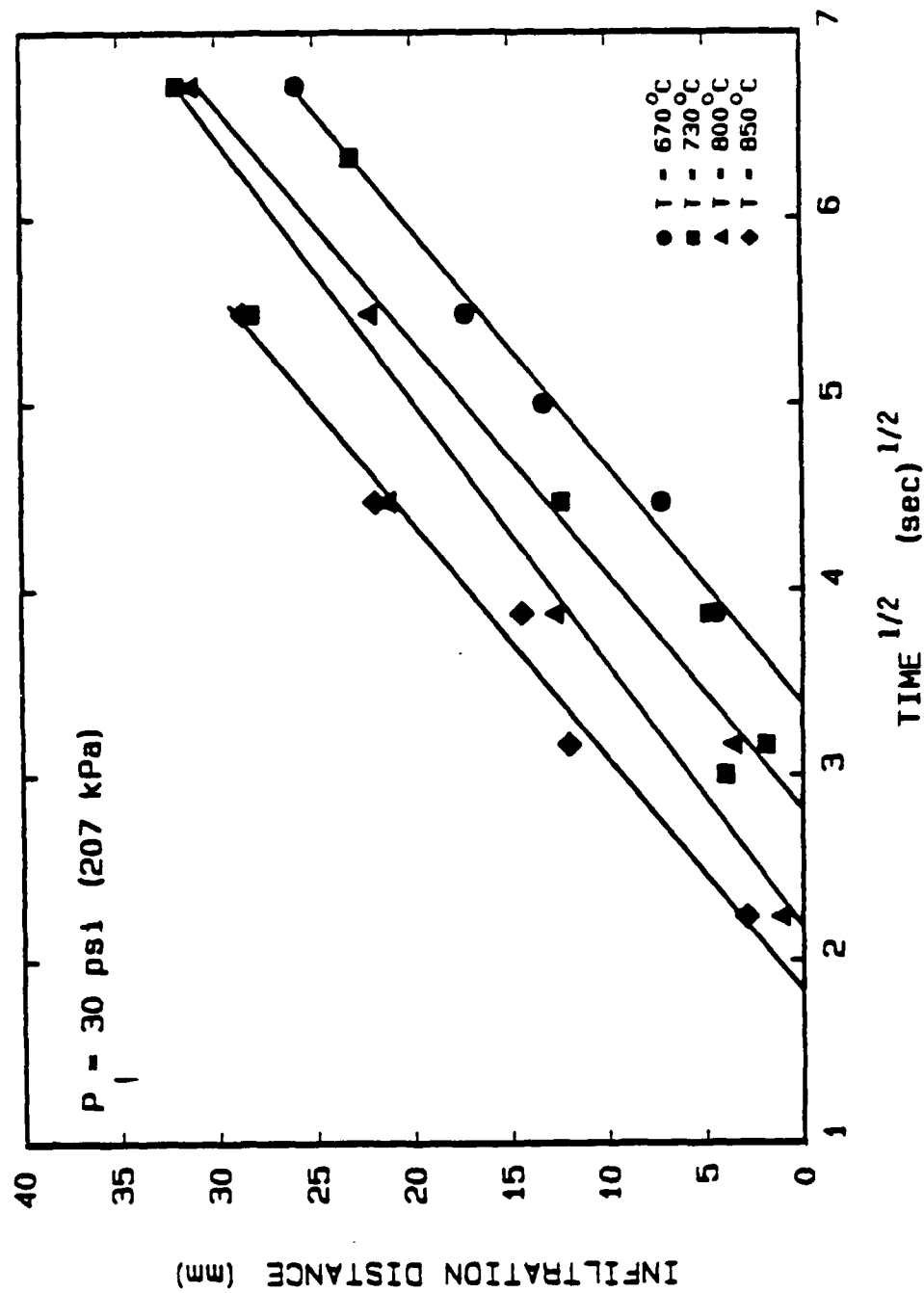
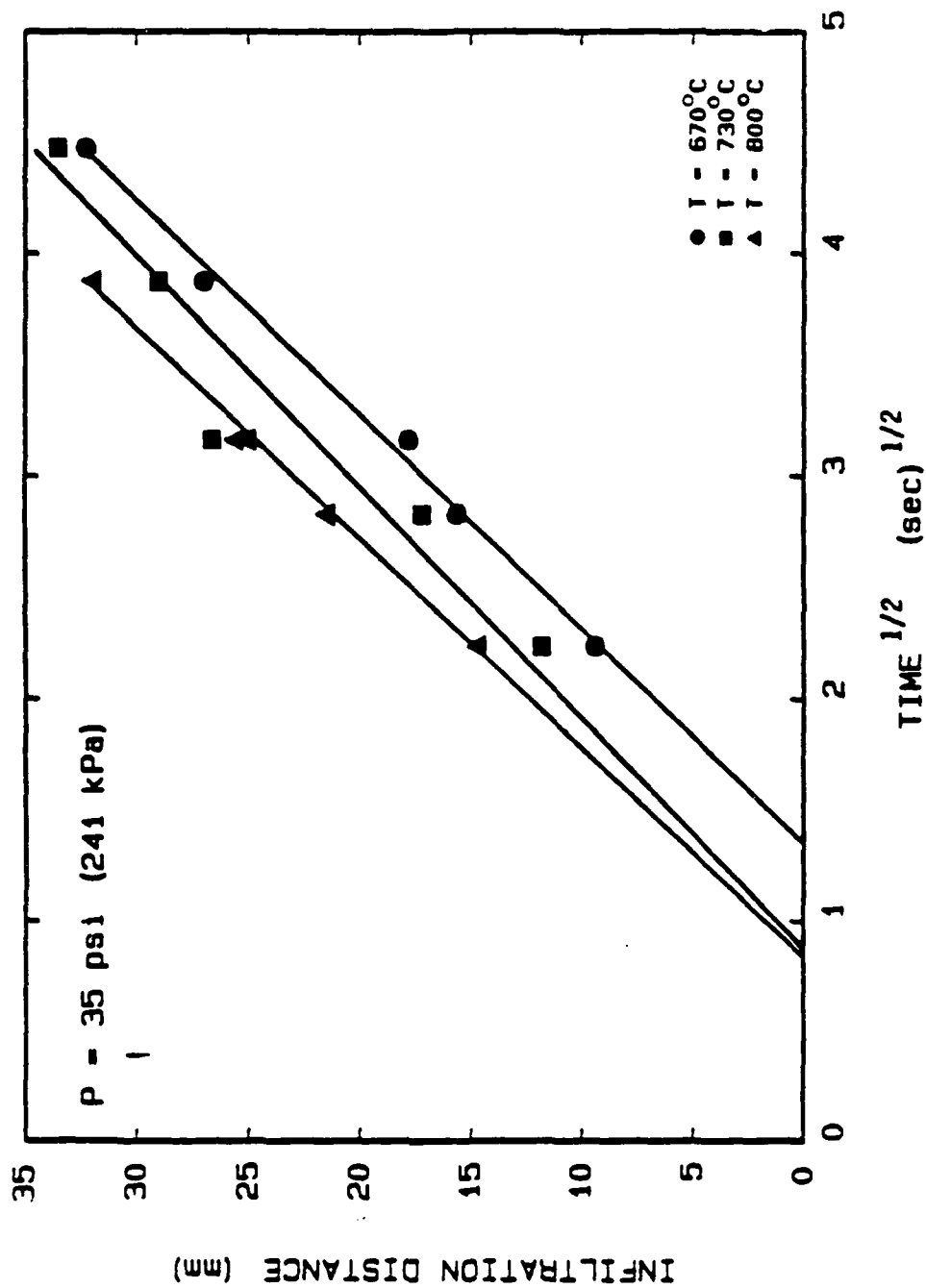Figure 1.4 Infiltration distance versus $(time)^{1/2}$ for aluminum in SiC at 35 psi (241 kPa).
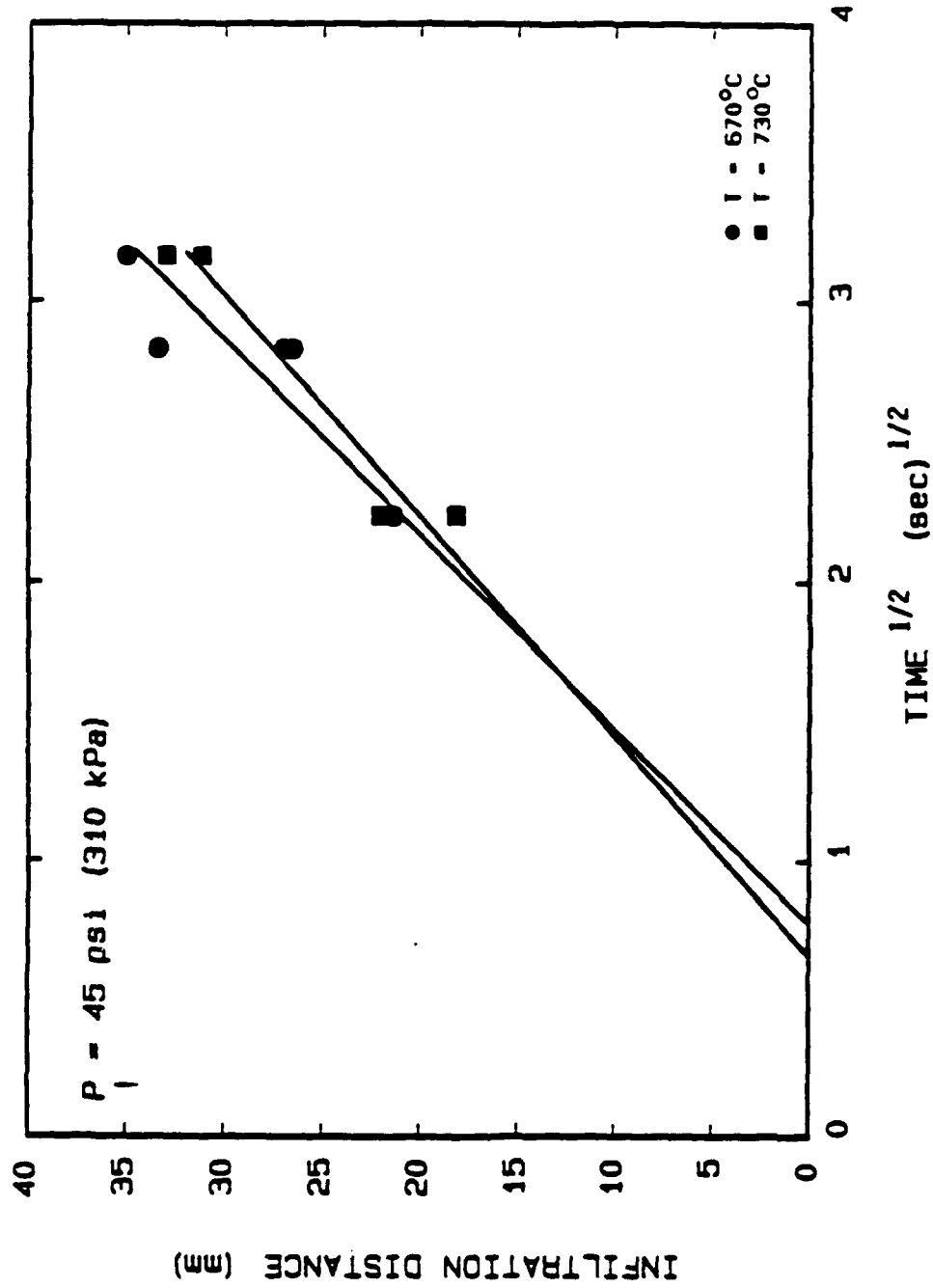
Figure 1.5   Infiltration distance versus (time)$^{1/2}$ for aluminum in SiC at 45 psi (310 kPa).

Assuming the preconditioning reaction to be of first order, an Arrhenius equation can be used to calculate the activation energy:

$$1/t_o = A [\exp (-Q/RT)] \tag{1.1}$$

where: t_o = incubation time, A = pre-exponential factor, R = gas constant, T = absolute temperature (°K).

It is apparent from the above equation that the thermal activation energy (the value Q in Eqn. 1.1) can be obtained from a semi-log plot of pre-conditioning rate (1/t) versus inverse temperature (1/T), as shown in Fig. 1.6. The activation energy was calculated to be 14.1 kcal./mole. The constant 'A' in the equation represents a normalized pre-conditioning rate that does not depend on temperature.

The rate of pre-conditioning was found to depend sensitively on the pressure of infiltration. The pressure dependence is shown clearly in Fig. 1.7, where the pre-conditioning rate, normalized by the temperature dependence (Eqn. 1.1) is plotted versus the applied pressure. Clearly, pressures in excess of 30 psi (207 kPa) strongly increased the incubation rate. In an attempt to quantify this dependence, the experimental data were compared to an equation of the form:

$$1/t_o = k \Delta P^n \tag{1.2}$$

A log-log plot of normalized rate of pre-conditioning versus infiltration pressure (Fig. 1.8) was constructed to determine the exponent

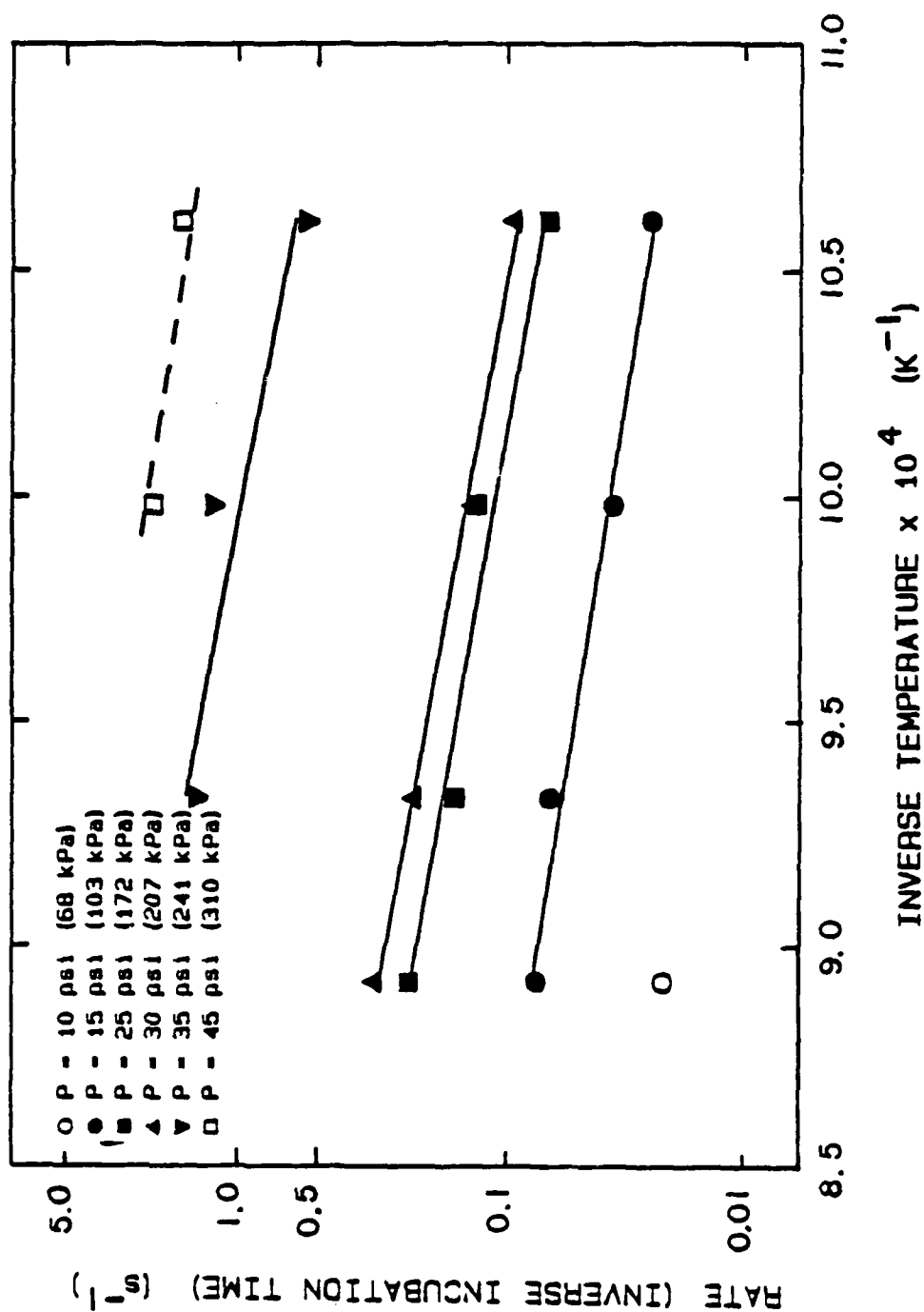Figure 1.6   Arrhenius plot of rate versus inverse temperature at different applied pressures.
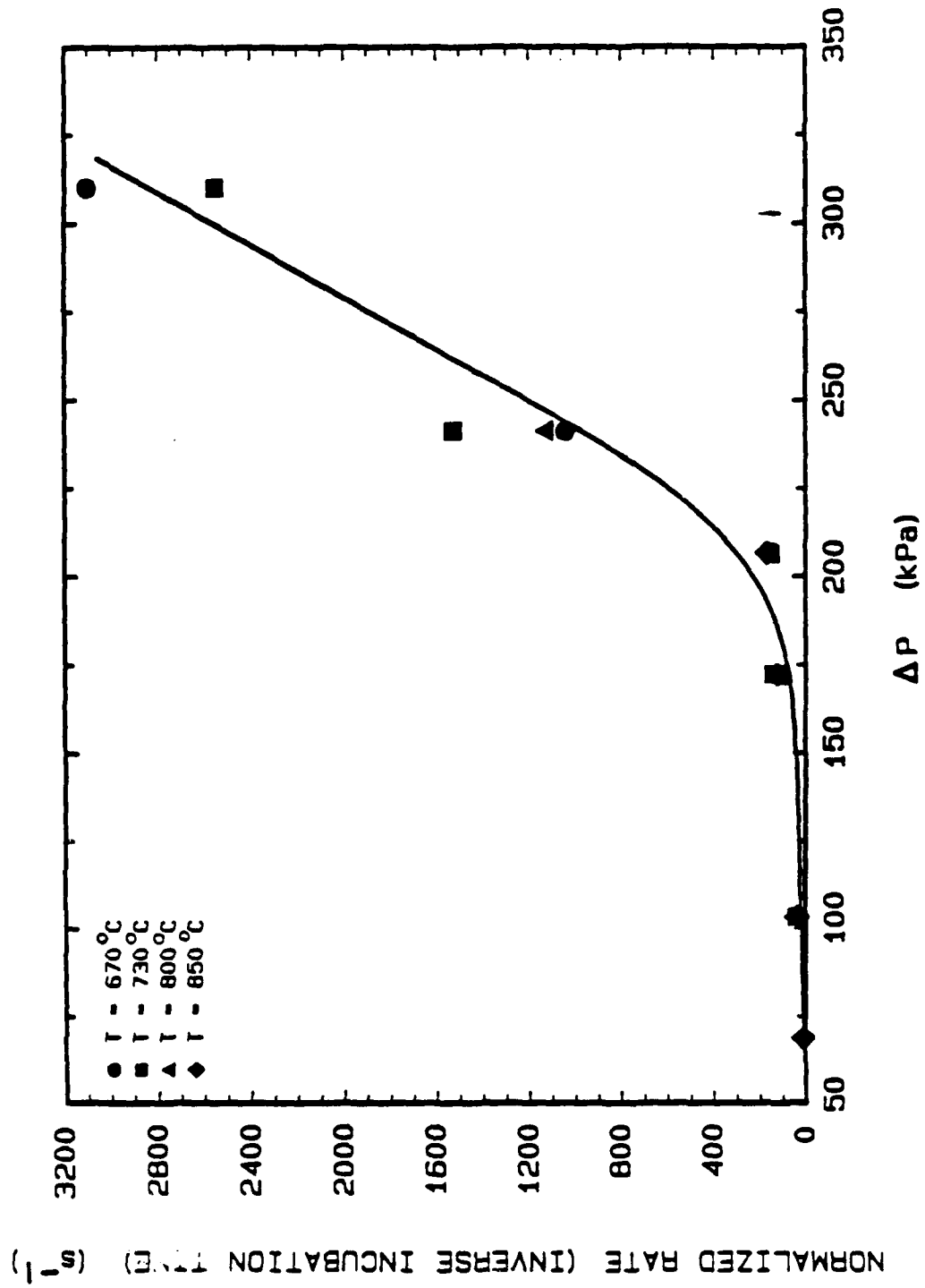
Figure 1.7 Temperature independent normalized rate versus applied pressure for aluminum in SiC.
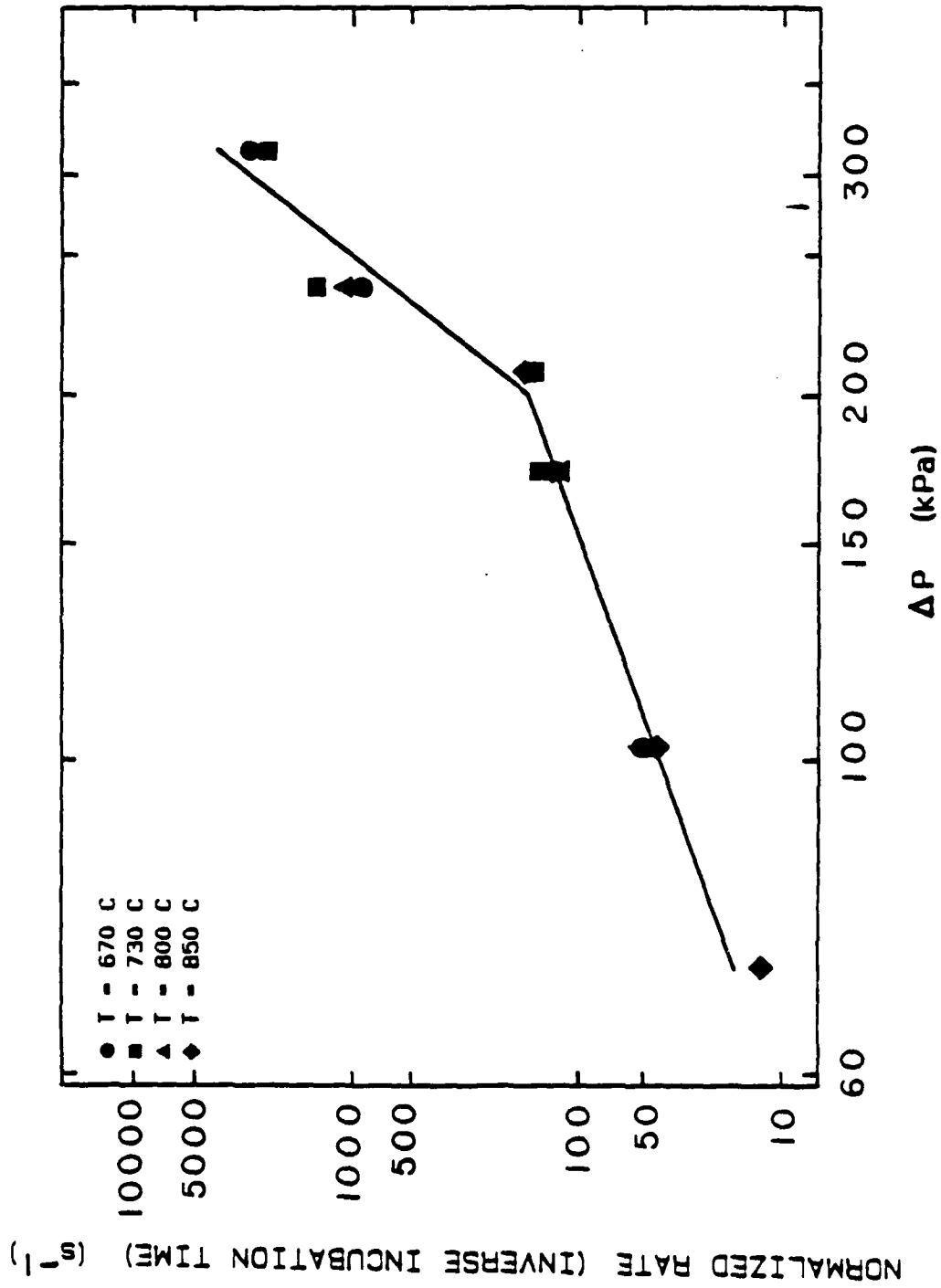
Figure 1.8   Normalized rate versus applied pressure on a natural logarithm plot. Used to determine exponent in Equ. 1.2.

n in Eqn. 1.2. Two distinct regimes of pressure dependence can be inferred from this plot. For applied pressures lower than 30 psi. (207 kpa), the exponent was estimated to be 2.9. However, for applied pressure greater than 30 psi (207 kpa) the pressure exponent was found to be 7.2.

1.2.2 Infiltration Studies

The parabolic time dependence of infiltration was theoretically addressed in the work of Martins, et al. (3), and has been verified experimentally by Maxwell (4) and Seitz (5):

$$h = A \ t^{1/2} \tag{1.3}$$

where h = infiltration distance, A = constant, and t = time.

Theoretical analysis (3) shows the constant 'A' in the above equation to be given by:

$$A = (2/K_1 \eta)^{1/2} \ (\Delta P - P_{th})^{1/2} \tag{1.4}$$

where, k_1 = constant related to the porosity of the compact and the particle diameter, and P_{th} = threshold pressure. The threshold pressure is that dynamic value of applied pressure required to overcome the wetting resistance and the fluid static head after infiltration has begun, and is not to be confused with the pressure required to negate incubation.

Equation 1.3 was used to experimentally estimate the threshold pressure. The value A, taken from the infiltration distance versus $(time)^{1/2}$ plots (Figs. 1.1-1.5), was plotted against the infiltration

pressure. Using the slope and intercept from these plots (Fig. 1.9) the
threshold pressures for different temperatures were calculated. The
temperature dependence of threshold pressure is shown in Fig. 1.10.

This temperature dependence can be rationalized by assuming that the
infiltration front proceeds with the establishment of a localized
equilibrium between the aluminum liquid and the SiC substrate:

$$Al_{(1)} + SiC = Al/SiC \qquad\qquad (1.5)$$

At equilibrium, Gibbs free energy for the reaction can be related to an
equilibrium constant K:

$$\Delta G^{O} = -RT \ln (K) \qquad\qquad (1.6)$$

where the constant K is inversely proportional to the partial pressure of
aluminum:

$$K = k'/P_{Al} \qquad\qquad (1.7)$$

The partial pressure of aluminum can be assumed to be proportional to
the threshold pressure:

$$P_{Al} \; \alpha \; P_{th} \qquad\qquad (1.8)$$
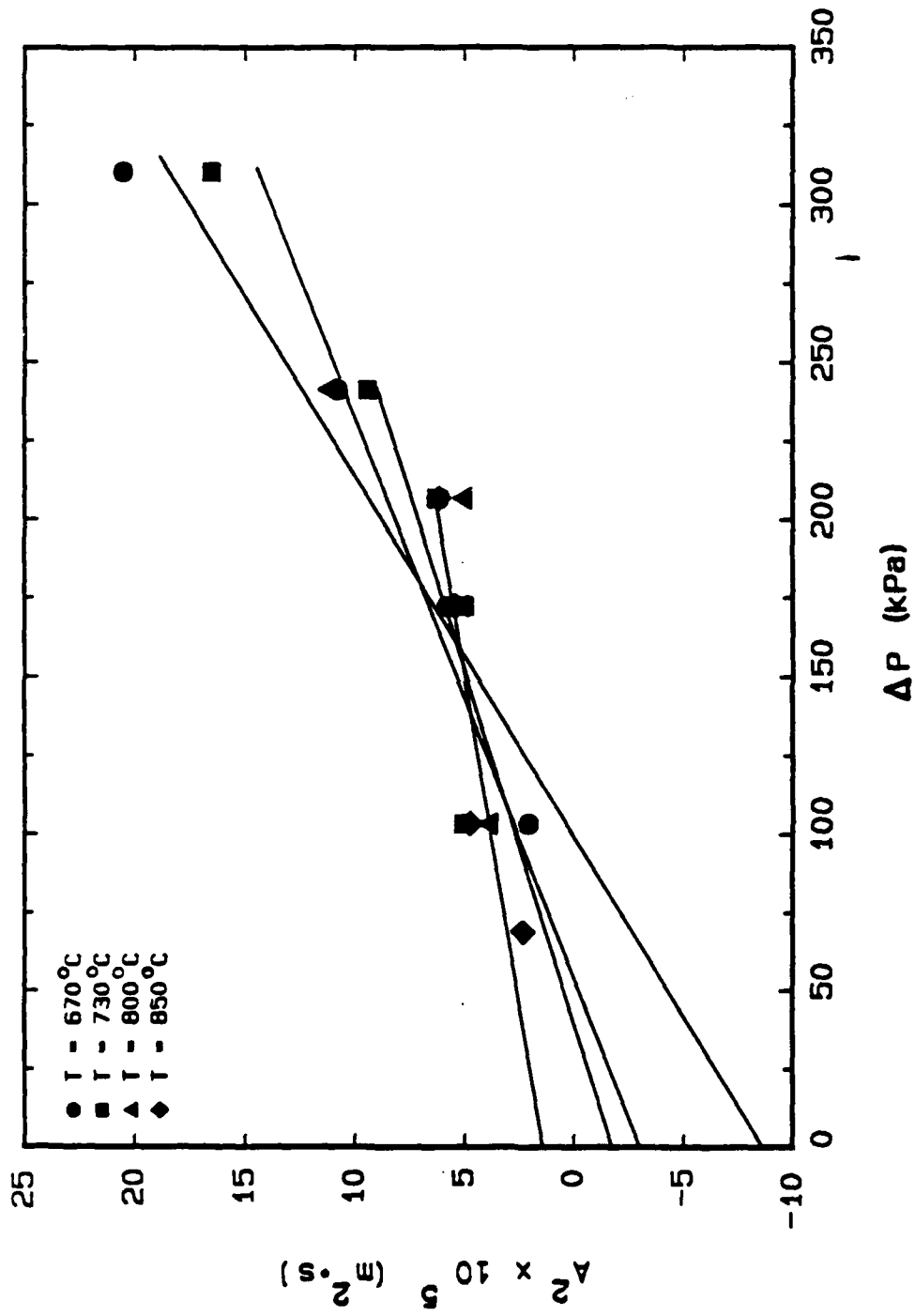
Figure 1.9 A^2 versus applied pressure.   A is the infiltration rate
parameter according to Equ. 1.3.
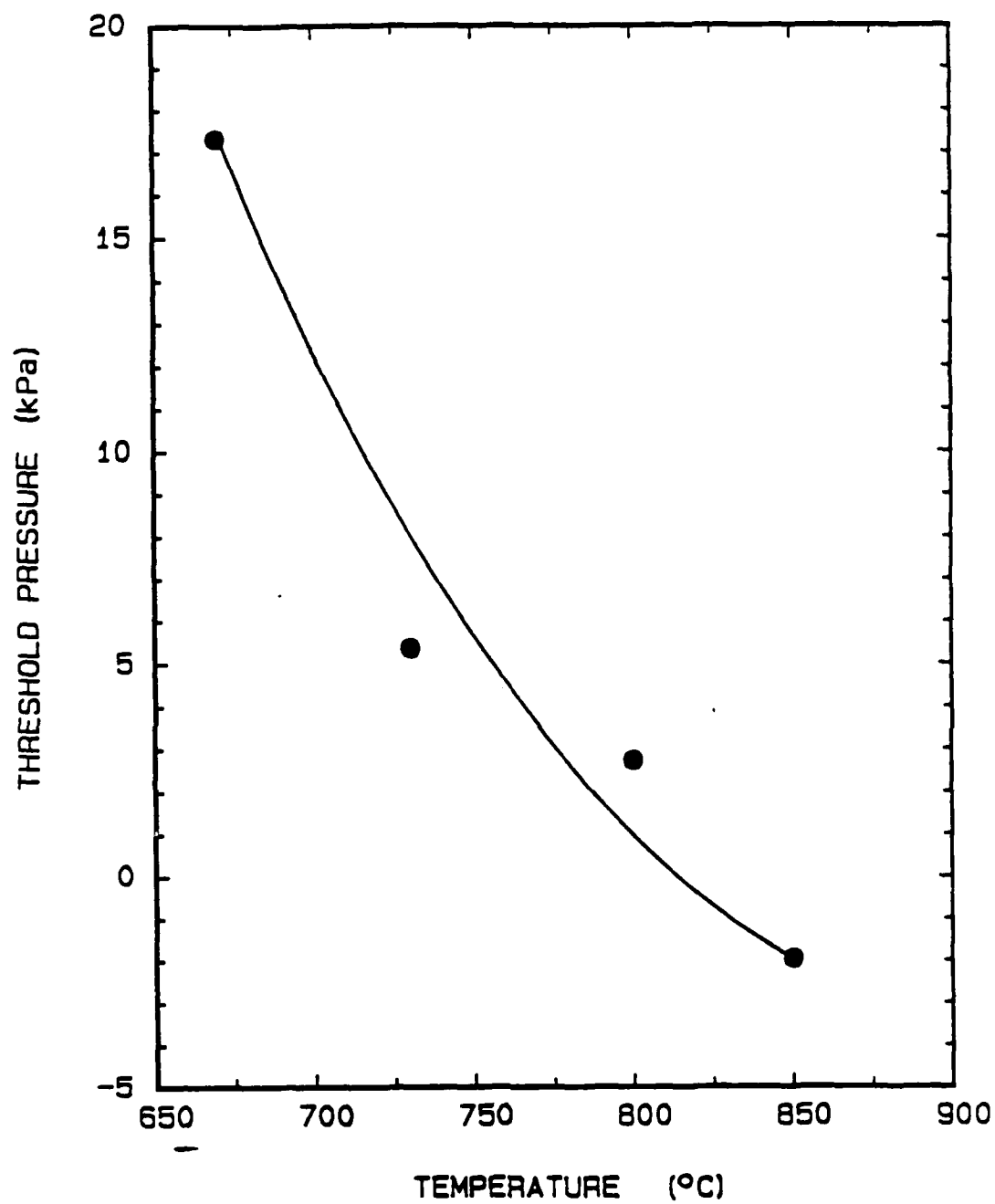
Figure 1.10   Temperature dependence of threshold pressure.

Therefore,

$$\Delta G^o = -RT \ln (k'/P_{th}) \qquad (1.9)$$

If ΔG_o is assumed to be linearly dependent on temperature the following temperature dependence for threshold pressure is predicted:

$$\ln (P_{th}) = a_1 + a_2/T \qquad (1.10)$$

Figure 1.11 shows the semi-logrithm plot of P_{th} versus inverse temperature.

1.3 Conclusions

In conclusion, the results from this study can be summarized as follows:

1. The incubation process for infiltration of silicon carbide particles with aluminum obeys the phenomenological equation:

$$Rate = \Delta P^n [\exp(-Q/RT)]$$

where: $n = 2.9$ (10 psi $\leq \Delta P \leq$ 30 psi)

$n = 7.2$ (30 psi $\leq \Delta P \leq$ 45 psi)

$Q = 14.1$ kcal/mole
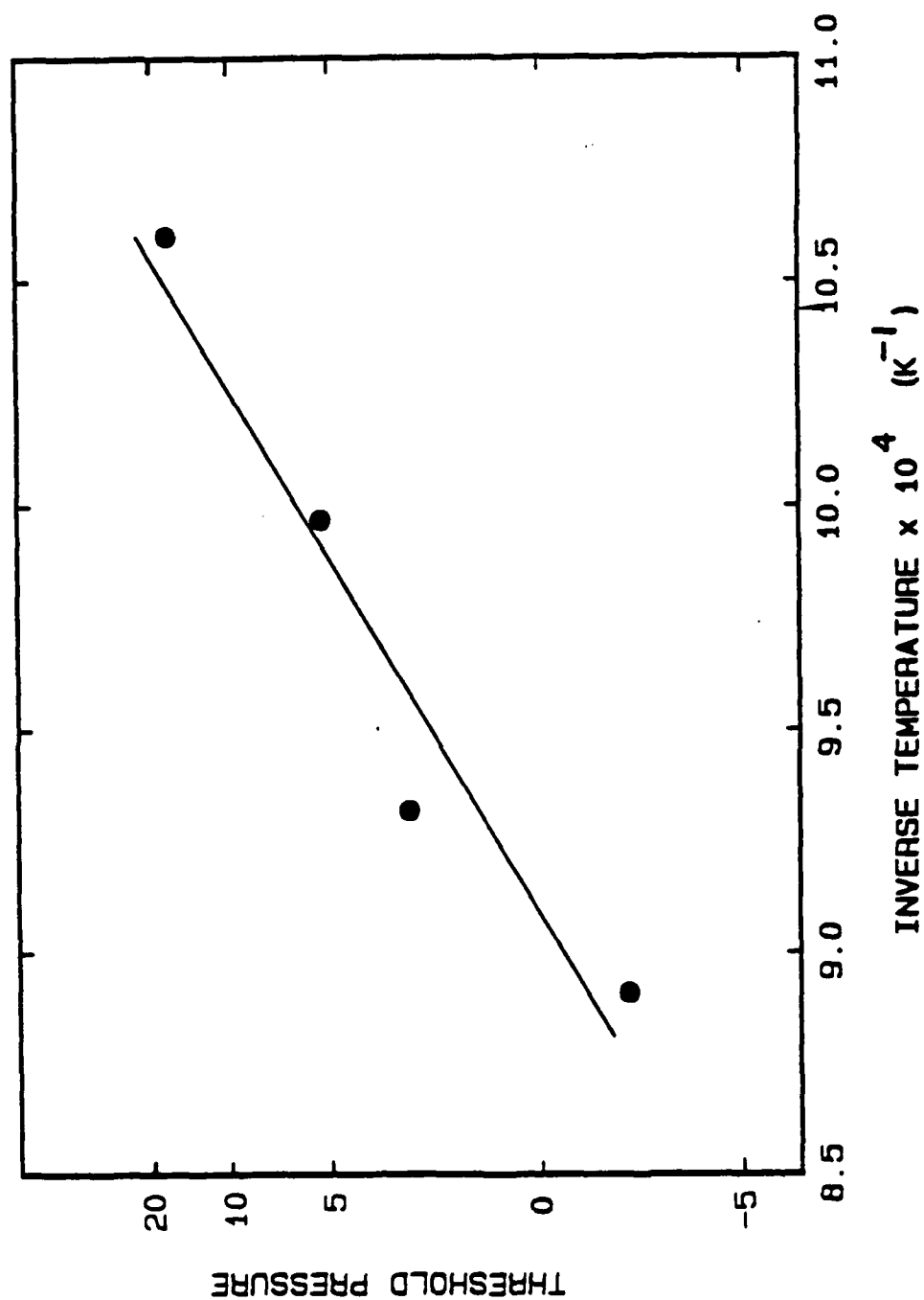
Figure 1.11 Threshold pressure versus inverse temperature.

2. The observations which characterize the incubation phenomenon are consistent with capillarity-driven aluminum vapor condensation, which pre-conditions the silicon carbide surfaces at the infiltration front.

3. The threshold pressure for infiltration of silicon carbide particles with aluminum is temperature sensitive, varying from 17.3 kPa at 670°C to zero at 850°C.

4. The temperature dependence of the threshold pressure can be expressed by the form:

$$\ln(P_{th}) = a_1 + a_2/T$$

1.4 References

1. Edwards, G.R., and Olson, D.L., "The Infiltration Kinetics of Aluminum in Silicon Carbide Compacts", Annual Report No. MT-CWR-087-032, Colorado School of Mines, July, 1987.

2. Edwards, G.R., and Olson, D.L., "Investigation into the Infiltration Kinetics and Interfacial Bond Strength of Al/SiC Composites", Annual Report No. MT-CWR-088-022, Colorado School of Mines, July, 1988.

3. Martins, G.P., Olson, D.L., and Edwards, G.R., "Modeling of
    Infiltration Kinetics fo Liquid Metal Processing of Composites",
    Metallurgical Transactions, vol. 19B, (1988), pp. 95-111.

4. Maxwell, P.B., "The Infiltration Behavior of Aluminum into Silicon
    Carbide Compacts", CSM Thesis No. T-3396, Colorado School of Mines,
    April, 1987.

5. Seitz, J.D., "The Infiltration Kinetics of Silicon Carbide Reinforced
    Aluminum Matrix Composites", CSM Thesis No. T-3614, Colorado School
    of Mines, December, 1988.

2.0 WETTABILITY MEASUREMENTS

2.1 Previous Results

The experimental setup and the methodology used for surface tension measurements are described elsewhere (1). Measurements of $\gamma^{lv}\cos\theta$ for pure aluminum and various aluminum alloys were previously reported (1), and are shown again in Fig. 2.1. Each point on the plot represents an average of at least five tests; the experimental scatter for each data point is within the dimensions of the symbol and error bands are therefore not shown. All of the metal/ceramic systems shown are non-wetting, and hence $\gamma^{lv}\cos\theta$ is negative.

The dashed lines represent $\gamma^{lv}\cos\theta$ for $Al_{(1)}$ on SiC and $Al_{(1)}$ on SiO_2 as calculated from measured values of γ^{lv} and contact angles found in the literature. Since SiC is reported to oxidize and form SiO_2, it is not unreasonable to assume that the macroscopic surface of SiC assumes a combination of both SiO_2 and SiC regions. Our measured $\gamma^{lv}\cos\theta$ values of pure aluminum on SiC lie between the calculated values for pure aluminum on SiC and the value for aluminum on SiO_2.

Except for the Al-Bi alloy, the magnitude of $\gamma^{lv}\cos\theta$ decreases with increasing temperature. As compared to pure aluminum at a given temperature, the additions of lithium and magnesium decrease the magnitude of $\gamma^{lv}\cos\theta$, whereas silicon has little effect on $\gamma^{lv}\cos\theta$. Though γ^{lv} decreases with increasing temperature for most metals, and can also decrease with increasing solute additions of a lower surface tension (according to the Gibbs absorption isotherm),
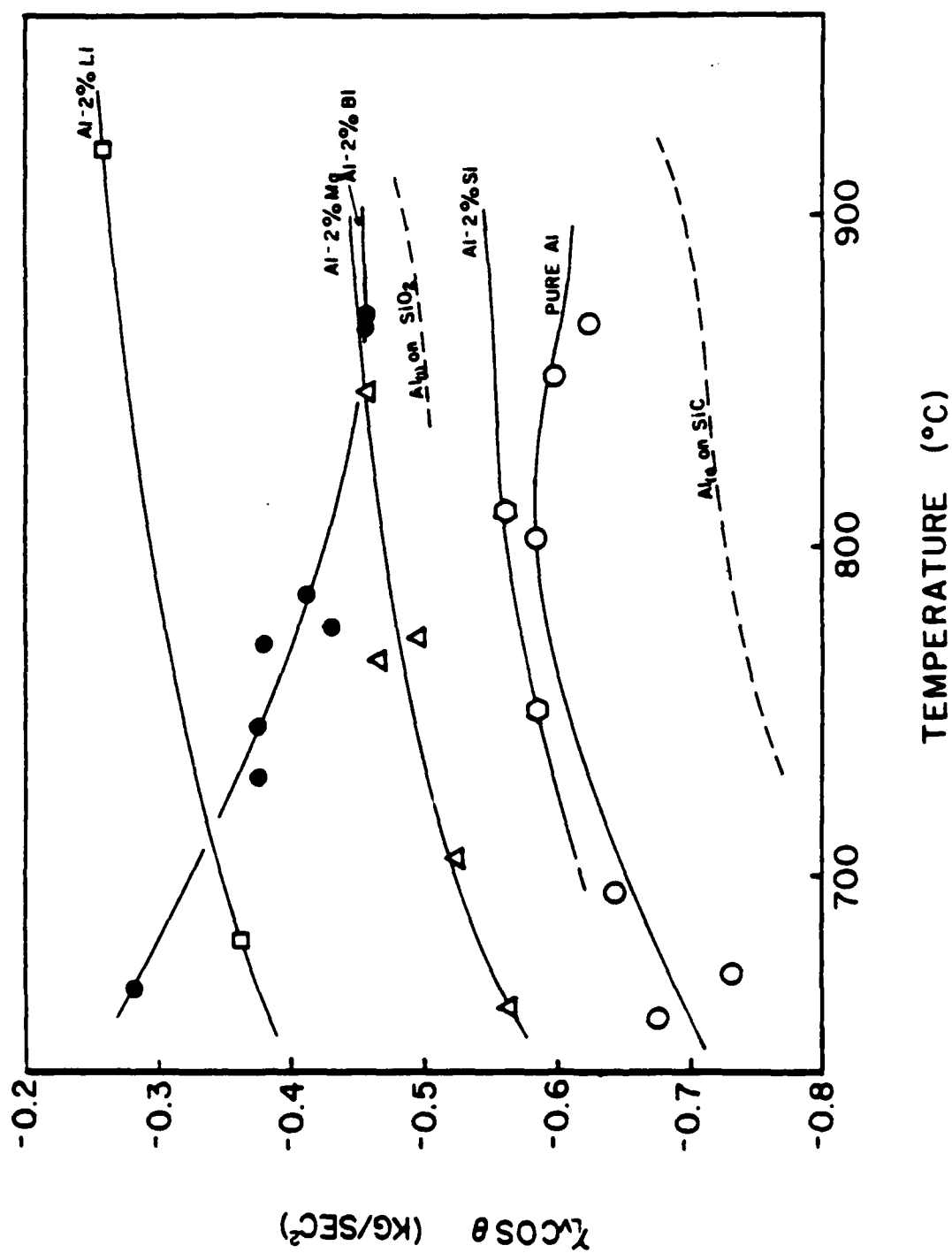
Figure 2.1 Wetting tendency ($\gamma_{LV}\cos\theta$) versus temperature for various aluminum alloys in SiC.

additions of lithium and magnesium to pure aluminum increase the tendency of the melt to wet the SiC surface.

2.2 Theoretical Development of $\gamma^{lv}\cos\theta$

The general cases for a liquid metal in contact with a ceramic substrate are shown in Figs. 2.2(a) and 2.2(b). Wetting and non-wetting refer to the situations where θ, the contact angle, is either less than 90° (the former) or greater than 90° (the latter). A balance of the surface tension forces shown in Fig. 2.2 results in the familiar Young equation:

$$\gamma^{lv}\cos\theta = \gamma^{sv} - \gamma^{sl}$$

In this equation, γ^{lv}, γ^{sv}, and γ^{sl} are the corresponding surface tensions (surface free energies) for the liquid/vapor, solid/vapor, and solid/liquid interfaces respectively. The conventional approach is to measure γ^{lv}, θ, and γ^{sv} and determine γ^{sl} from the difference.

In this study, $\gamma^{lv}\cos\theta$ is measured directly by the technique of capillary rise and then compared to the derived quantities of γ^{sv} and γ^{sl}. The γ^{sv} value is related to the cohesive energy of a compound, and can be indirectly determined from optical absorption measurements for ceramic compounds, as discussed in Section 3.0 of this report. Values for γ^{sv} are difficult to measure experimentally. Therefore, the calculations made in this report are limited to values available in the literature (2).

- WETTING ($\theta < 90$, $\gamma^{SL} < \gamma^{SV}$)
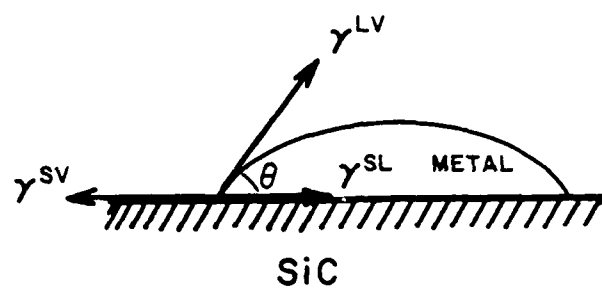
a)

- NON-WETTING ($\theta > 90$, $\gamma^{SL} > \gamma^{SV}$)
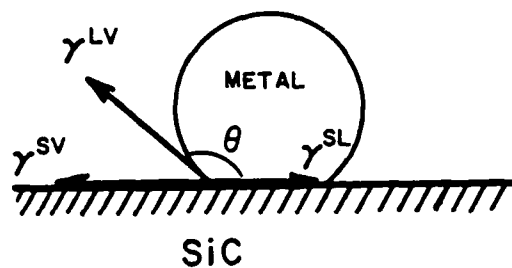
$$\gamma^{LV} COS\theta = \gamma^{SV} - \gamma^{SL}$$

. b)

Figure 2.2   Liquid metal on ceramic substrate.   a) wetting, b) non-wetting.

Theoretical discussions of the interfacial energy between a clean liquid metal and a clean solid ceramic material are not thoroughly developed. Miedema (3) presents a fundamental interpretation of γ^{sl} for liquid metals in contact with solid metals and this analysis will provide a basis for metal/ceramic material interfaces. According to Miedema, γ^{sl} is comprised of three terms:

1) γ_1^{sl} - enthalpic contribution of the crystal (solid)

2) γ_2^{sl} - Entropy decrease caused by ordering of liquid
   atoms near the solid interface.

3) γ_3^{sl} - chemical interaction between melt and crystal

The earliest account of γ^{sl} is from Skapski (4), where γ_1^{sl} is proportional to the latent heat of melting; e.g. a fraction of the surface atom's bonding is structurally disordered, similar to concepts of a liquid, rather than crystal bonding and is included in the γ^{sl}. Ewing (5) later incorporates another term γ_2^{sl}, to account for the entropy deficit of the melt in the region of the interface. Although the first two terms can adequately predict interfacial energies for pure metals in contact with their own melts, another term, γ_3^{sl}, has to be included in the dissimilar metal case to account for any possible interaction effects.

Miedema successfully described this interaction effect for the dissimilar metal case by relating γ_3^{sl} to the enthalpy of mixing, ΔH_m. Since a number of metal binary systems follow 'regular' solution theory and exhibit reasonable mutual solubility in the other

component, the predicted γ^{sl} values of Miedema were in good
agreement with the measured values.

For liquid metals in contact with solid ceramics, the interaction
parameter is more adequately described in terms of the enthalpy of
reaction since mutual solubilities are very low. A positive contribution
relates to an endothermic reaction (no interaction), and a negative
contribution relates to an exothermic reaction (favorable interaction).

The effect of this interaction term is best understood in the context
of the $\gamma^{lv}\cos\theta$ expression. Substituting in all the terms for
γ^{sl};

$$\gamma^{lv}\cos\theta = \gamma^{sv} - [C_1 \left(\frac{L_f}{V_m^{2/3}} + \frac{\Delta H_f}{V_m^{2/3}}\right) + C_2 \frac{T}{V_m^{2/3}}]$$

For a given ceramic substrate and temperature, γ^{sv} and L_f of
the crystal are independent of the contacting molten metal. Likewise, the
magnitude of the 'entropy term', $C_2 T/V_m$, is a function of the molten
metal and not the type of solid substrate. If the theoretical development
is correct, the magnitude and sign of $\gamma^{lv}\cos\theta$ is strongly
affected by the interaction term, ΔH_f.

As an example, consider the aluminum liquid/silicon carbide crystal
system at 1000°K. A measured value for the γ^{sv} of β-SiC is
2180 mJ/m^2 (6). Theoretically calculated values for different SiC faces
(planes) range from 2600 to 5300 mJ/m^2 (7). An assumed value of 3000
mJ/m^2 for a SiC surface that contains fine-grained, randomly oriented
crystals is used for this exercise.

The enthalpy term, L_f, is related to the latent heat of fusion of the crystal. SiC does not melt, but rather dissociates or decomposes into solid graphite and liquid silicon at 3280°K. The enthalpy of decomposition for this reaction is 27.9 kcal/mole (8). Since the test temperature of 1000°K is well below the SiC decomposition temperature, an extra enthalpy term is included which is proportional to the heat capacity, $H_{m.p.}$ - H_T. The calculated enthalpy contribution from the crystal then is 1094 mJ/m^2.

The entropy deficit contribution from the aluminum melt is related to the temperature and the molar volume of the aluminum. This contribution is on the order of 112 mJ/m^2.

Finally, for the interaction parameter, assuming limited solubility and the following chemical reaction with pure aluminum liquid;

$$4Al_{(1)} + 3SiC_{(s)} \longrightarrow Al_4C_3 + 3Si_{(1)} \quad \Delta H_f = 24.2 \text{ kcal/mole}$$
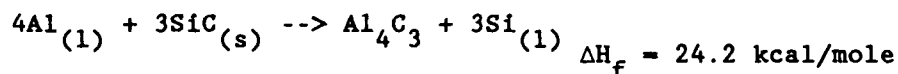
The calculated $\gamma^{1v}\cos\theta$ would be:

$$\gamma^{1v}\cos\theta = 3000 - (1094+112+163) = 1631 \text{ mJ/m}^2$$

Using γ^{1v} and contact angle measurements from the literature (9), $\gamma^{1v}\cos\theta$ is not only smaller than the calculated 1631 mJ/m^2 (about half), but of the opposite sign. The measured contact angles are greater than 90°, the $\gamma^{1v}\cos\theta$ term is therefore negative.

A more plausable interpretation for the above interaction parameter is to assume that an aluminum oxide is present rather than pure molten aluminum.

Hence, the chemical reaction would be:

$$Al_2O_3 + 3/2 \ SiC_{(c)} \rightarrow 1/2 \ Al_4C_{3(c)} + 3/2 \ Si_{(1)} + 3/2 \ O_{2(g)}$$

$$\Delta H_f = 390 \ kcal/mole \rightarrow \gamma_3^{sl} = 2632 \ mJ/m^2$$
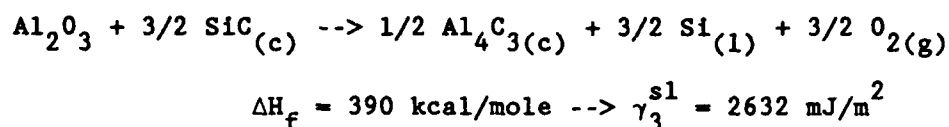
and $\gamma^{lv}\cos\theta = 3000 - 3839 = -839 \ mJ/m^2$.

The calculated value agrees with the measured γ^{lv} and $\cos\theta$ values from the literature (10).

In metal/ceramic systems, a major contribution to the $\gamma^{lv}\cos\theta$ term can come from the chemical interaction term, whether it be a positive, non-wetting contribution (i.e. endothermic) or a negative, wetting contribution (exothermic). The incorporation of a chemical interaction term into the γ^{sl} expression is not surprising since it has been suggested (11) that good wetting is favored by the formation of chemical bonding at the interface.

2.3 Discussion

2.3.1 Pure Aluminum

The calculated value of $\gamma^{lv}\cos\theta$ for aluminum on SiC at 1000°K is presented in Section 2.2 which suggests that the measured values of $\gamma^{lv}\cos\theta$ from the literature (9) evaluate aluminum oxide in contact with SiC rather than pure aluminum metal in contact with

a SiC substrate. The calculated value of -839 mJ/m^2 agrees fairly well

with the measured value of -630 mJ/m^2 in this investigation.

Considering the value of γ^{sv} (SiC) assumed in the calculation, the

agreement is reasonable.

2.3.2 Magnesium Addition

Because γ^{lv} for liquid magnesium is less than γ^{lv} for

liquid aluminum, magnesium should preferentially segregate to the surface

of the aluminum. If pure magnesium were to react with silicon carbide at

1000°K, magnesium silicide is thermodynamically more stable than

magnesium carbide. However, in the presence of oxygen at the surface of

the melt, magnesium oxide would form, and the following solid/liquid

chemical interaction is projected:

$$2MgO + SiC \longrightarrow Mg_2Si + C + O_2$$
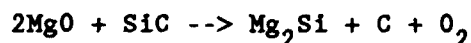
$$\Delta H_f = 286 \text{ kcal/mole} \longrightarrow \gamma^{sl} = 3762 \text{ mJ/m}^2$$

and hence, $\gamma^{lv}\cos\theta = 3000 - 3762 = -762$ mJ/m^2. The measured

value of $\gamma^{lv}\cos\theta$ at 1000°K for a 2 wt. pct. magnesium

addition was -515 mJ/m^2.

2.3.3 Lithium Addition

Just as magnesium segregates to the surface of liquid aluminum,

lithium will also segregate to the surface of aluminum. In the presence

of lithium at 1000°K, silicon carbide will react to form a lithium

carbide as opposed to a lithium silicide. With oxygen at the metal surface, the following chemical interaction would occur:

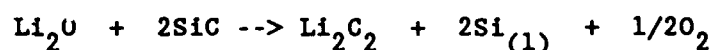$$Li_2O + 2SiC \rightarrow Li_2C_2 + 2Si_{(1)} + 1/2O_2$$

$$\Delta H_f = 186.5 \text{ kcal/mole} \rightarrow \gamma^{sl} = 3600 \text{ mJ/m}^2$$

and therefore, $\gamma^{lv}\cos\theta = 3000 - 3600 = -600 \text{mJ/m}^2$. The measured $\gamma^{lv}\cos\theta$ value for an Al-2% Li alloy was -340 mJ/m^2.

2.3.4 Silicon Addition

The addition of silicon to liquid aluminum is considered to only affect the activity of liquid silicon in the following reaction:

$$Al_2O_3 + 3/2SiC \rightarrow 1/2Al_4C_3 + 3/2Si_{(1)} + 3/2 \, O_s$$
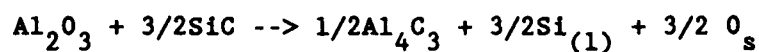
As the activity of liquid silicon is increased, the formation of aluminum carbide is less favored (i.e. equilibrium shifted to the left or the reactants side). The addition of silicon should not affect the enthalpy of formation of the reaction and hence, the response of the Al-2% Si alloy should be similar to that of the pure aluminum. Referring to Fig. 2.1, the measured $\gamma^{lv}\cos\theta$ for the Al-2% Si alloy is nearly the same as the measured $\gamma^{lv}\cos\theta$ for pure aluminum. The measured values of $\gamma^{lv}\cos\theta$ at 1000 K for pure aluminum and the aluminum alloys are shown in Table 2.1 along with the calculated values.

TABLE 2.1 - $\gamma^{lv}\cos\theta$ of Molten Aluminum on α-Sic
$(\gamma^{sv} = 3000 \text{ mJ/m}^2)$

| Molten Metal | CALCULATED (1000°K) | | MEASURED |
	γ^{sl} (mJ/m^2)	$\gamma^{lv}\cos\theta$ (mJ/m^2)	$\gamma^{lv}\cos\theta$ (mJ/m2)
Pure Aluminum	1370	1630	
Aluminum Oxide	3839	-839	-630
Aluminum/Magnesium	3762	-762	-515
Aluminum/Lithium	3600	-600	-340

2.3.5 Oxidation of SiC Crystal

In the event a stable oxide were to form on the SiC surface, the
interfacial reaction would then be for aluminum on a quartz substrate.
For SiO_2, the γ^{sl} term, or enthalpy contribution from the crystal,
would relate to the melting of SiO_2. At 1000°K, the value for
γ^{sl} is 235 mJ/m^2. Assuming oxygen is present at the liquid
surface, the following reaction for aluminum oxide on quartz is suggested:

$$Al_2O_3 + SiO_2 \longrightarrow SiAl_2O_5 \quad \Delta H_f = -2 \text{ kcal/mole} \longrightarrow \gamma^{sl} = 331 \text{ mJ/m}^2$$
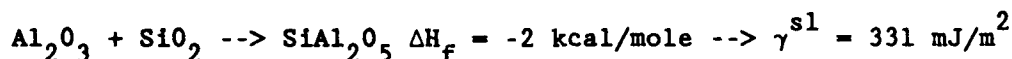
Since the reported (1) surface free energy for SiO_2 is approximately 300
mJ/m^2, $\gamma^{lv}\cos\theta = 300 - 331 = -31$ mJ/m^2; a non-wetting
system. The corresponding contact angle for $\gamma^{lv}\cos\theta = -31$
mJ/m^2 is ~92°. In the literature (12), a contact angle of 126°
has been given for the aluminum/quartz system. If a less stable product,
such as a spinel, were to be proposed in the above reaction, as opposed to
the aluminate, $SiAl_2O_5$, then the calculated contact angle would be
greater and in closer agreement with the measured values.

Considering the applicability of bulk thermodynamic quantities to the
calculation of interfacial reactions, the proposed thermodynamic
evaluation of the aluminum/silicon carbide interface is plausible. The
magnitude of the calculated interfacial surface tension and
$\gamma^{lv}\cos\theta$ term are in reasonable agreement with the measured
values in this investigation. This technique can be extended to other
metal/ceramic systems, such as transition metal/saphire interfaces, where
interfacial compounds such as spinels are known to form.

2.4 Conclusions

The conclusions from this analysis for the wetting of aluminum on α-SiC are as follows:

1) Interfacial surface tension is strongly influenced by the oxidation of aluminum.

2) Alloying elements, such as Mg and Li with lower liquid/vapor surface tensions, lower the magnitude of the interaction parameter by changing the nature of the oxide at the interface.

3) In the event SiC oxidizes, the wetting of aluminum on SiC is enhanced (lower $\gamma^{lv}\cos\theta$).

2.5 References

1. Edwards, G.R., and Olson, D.L., "The Infiltration Kinetics of Aluminum in Silicon Carbide Compacts", Annual Report No. MT-CWR-087-032, Colorado School of Mines, 1987.

2. Tyson, W. R.;'Surface Energies of Solid Metals', Canadian Metallurgical Quarterly, V.14, No.4, (1975), p. 307.

3. Miedema, A. R., den Broeder, J.A.; 'On the Interfacial Energy in Solid-Liquid and Solid-Solid Metal Combinations', Z. Metallakund, V. 70, (1979), p. 14.

4.   Skapski, A. S., _Acta_ _Metall_., V.4, (1956), p.576.

5.   Ewing, R. H.; 'The Free Energy of the Crystal-Melt Interface from the
      Radial Distribution Function-Further Calculations', _Phil_. _Mag_., V.
      25, (1972), p. 779.

6.   Osheherin, B. N.; _Phys._ _Status_ _Solidi_ (_a_), V.34, (1976), K181.

7.   Takai, T., Halicioglu, T., and Tiller, W. A.; 'Reconstruction and
      Energetics for Surfaces of Silicon, Diamond and B-SiC', _Surface_
      Science, V.164, (1985), p. 341.

8.   Stull, D. R., and Prophet, H.;'JANAF Thermochemical Tables', 2nd
      Ed. NBS, 1970.

9.   Warren, R., and Andersson, C. H.; 'Silicon Carbide Fibres and Their
      Potential for Use in Composite Materials, Part II', _Composites_, V.
      15, No. 2, (1984), p. 101.

10.   Eustathopoulos, N.;'Energetics of Solid/Liquid Interfaces of Metals
      and Alloys', _International_ _Metals_ _Reviews_, V.28, No.4,(1983), p. 189.

11.   Delaney, F., Froyen, L., and Deruyttere, A., 'The Wetting of Solids
      by Molten Metals and its Relation to the Preparation of Metal-Matrix
      Composites'.

12. Warren, R., and Anderson, C.H., "Silicon Carbide Fibers and their Potential for Use in Composite Materials", Part II, <u>Composites</u>, vol. 15, no. 2, (1984), p. 101.

3.0 PREDICTIONS OF INTERFACIAL PROPERTIES

3.1 Introduction

There are many applications in advanced materials processing today where the joining of a ceramic to a metal, or the incorporation of a ceramic reinforcement into a metal matrix, is the single most important factor in controlling the ultimate performance of the finished product. These composite materials must often be processed without any real understanding of the mechanics or chemical interactions at the metal/ceramic interface. While predictive models, both theoretical and empirical, have been developed to describe atomic and bulk interactions between dissimilar materials, these models are either limited in scope or experimentally unsubstantiated.

The objective of this investigation was to predict, prior to fabrication, the interfacial bond strength of metal/ceramic composites, such as SiC/aluminum, in terms of measurable quantities. Hence, the approach was to develop a predictive model in terms of the free surface properties of the components at the interface and to corroborate predicted interfacial energies with actual measurements of interfacial properties.

3.1.1 The Concept of the Interfacial Bond Energy

The interfacial bond energy between compounds A and B, by construction, is proportional to the individual free surface energies and a chemical interaction energy.

The following simple energy expression, developed by Miedema (1) for metal/metal interactions, is applied to the general metal/ceramic case:

$$-\Delta\gamma_{AB}^{Bond} = 0.85 \ (\gamma_A^{s,o} + \gamma_B^{s,o}) - \gamma_{chem}^{ss} \qquad (3.1)$$

where: $\gamma_{chem}^{ss} = 2.5 \times 10^{-9} \ \dfrac{\Delta H_m^l}{v_i^{2/3}}$

and: ΔH_m^l = integral heat of mixing

V_i = molar volume

As illustrative examples, the calculated interfacial bond energies, $\Delta\gamma_i^{bond}$, between aluminum/aluminum free surfaces and copper/copper free surfaces, using the above relation, are given in Table 3.1. These calculated interfacial bond energies are compared to the approximate 'cohesive energy' of a plane (100) of atoms in the FCC unit cell. The trend in the calculated $\Delta\gamma_i^{bond}$'s is consistent with the internal cohesive energy calculations.

The interfacial bond energy then, depends on the measured quantities, $\gamma_i^{s,o}$ and γ_{CHEM}. For most metal/metal systems, γ_{CHEM}, is much less than the sum of the two surface free energies. For most metal/ceramic systems, the solubility of one component in the other is very low; however, the magnitude of γ^{ss} can be quite significant.

Thermodynamically, γ^{ss} is proportional to the enthalpy of compound formation at the metal-ceramic interface. Bulk thermodynamics is not a sufficient measure, however, of near surface thermodynamic behavior and careful consideration is necessary when selecting thermodynamic quantities from the literature. Metal/ceramic interfaces

TABLE 3.1 - Calculated Interfacial Bond Energies of
Al/Al and Cu/Cu Interfaces

Element	$\gamma_1^{s,o}$ $(\frac{J}{m^2})$	$-\Delta\gamma_1^{BOND}$ $(\frac{J}{m^2})$	Cohesive Energy (J/m^2)	%
Al	1.2	2.04	3.31	62
Cu	1.4	2.38	4.26	56

are characterized by low symmetry. Compounds which form in the interphase region tend to increase the symmetry and stability between the metal and the ceramic. Since strong metal/ceramic bonds will typically contain interface compounds that are more stable than either the metal or the ceramic near the interface, the near surface thermodynamic stability of the ceramic or the metal will affect metal/ceramic bonding (i.e. this suggests that disruption or destabilization of near surface properties of the ceramic can enhance metal/ceramic bonding).

The predictability of the interfacial bond strength in metal/ceramic systems is ultimately dependent upon the accuracy of this interaction term. Measurement of internal interfacial properties at near atomistic levels is experimentally difficult to obtain; however, the optical method outlined in this investigation is one approach. Metal-ceramic free surface energies and the chemical interaction term are to be discussed separately in subsequent sections.

3.1.2 Surface Free Energies

The surface free energies, $\gamma^{S,O}$, are difficult quantities to measure directly, although empirical correlations to bulk material properties, such as cohesive energy and heats of vaporization, have been developed. Conceptually, the surface energy is related to the bulk latent heat of vaporization, and adjusted for the reduced number of nearest neighbor atoms at a crystal surface.

The surface energy is also related to the behavior of electrons in the valence band region. As the nearest neighbor atomic environment

changes, through surface reconstruction or chemical interaction, the electronic energy levels shift and/or broaden accordingly. The shifts of the valence electron levels relate to changes in the overall interfacial energy. To measure valence band structure changes or transitions, which are on the order of 0.5-10 ev in metals and semiconducting materials, the magnitude of the excitation or incident energies must be at least in the optical region of the electromagnetic spectrum.

In this study, surface free energies for the ceramic and the metal are predicted from empirical relations that relate valence electron transitions to the cohesive energy or surface free energy of a compound. The cohesive energy relation for semiconductors (ceramics) is from Phillips and Van Vechten (2). The surface energy relation for metals was developed as part of this investigation and will be presented in the next section.

3.1.2.1 Surface Energy for Ceramics

According to Phillips for Group IV semiconductor (ceramic) compounds:

$$\text{cohesive energy} \quad \alpha \ \Delta G^{O} \ [1 - a^{-1/2} f_i(AB)] \tag{3.2a}$$

where: ΔG^{O} = scaling factor

a = lattice constant

$f_i(AB)$ = ionic ordering energy (ionicity)

The ionicity parameter is related to the dielectric function of the ceramic substrate or the optical absorption characteristics of the solid.

Using Phillips expression for cohesive energy, and realizing that surface energy is proportional to the cohesive energy of the solid, a surface energy expression for ceramic substrate would have the following form:

$$\gamma^{s,o} = \gamma^{o}[1 - a^{-1/2} f_i(AB)] \qquad (3.2b)$$

where γ^{o} = scaling factor similar to ΔG^{o}.

The above expression is an extension of Phillips work, but will provide a basis for measuring the 'average' surface energy of a ceramic substrate.

3.1.2.2 Interaction Parameter

In addition to the cohesive energy expression, Phillips developed an empirical expression for the enthalpy of formation of Group IV type compounds. Phillips' ΔH_f expression provides a basis for evaluating the 'chemical interaction' term of the interfacial bond (see Eqn. 3.1. According to Phillips:

$$\Delta H_{AB} = \Delta H_o \left(\frac{a_{Ge}}{a_{AB}}\right)^s [1 - b(\frac{E_2}{E})^2] f_i(AB) \qquad (3.3)$$

$\left(\dfrac{a_{Ge}}{a_{AB}}\right)$ = covalent energy not lost by dehybridization from d-levles (a_i = lattice constants)

$$[1 - b(\frac{E_2}{E})^2] = \text{metallization} \ (E_2 \text{ and } E \text{ refer to direct band gaps})$$

$f_i(AB)$ = ionic ordering energy (determined from dielectric constant)

Except for ΔH_o, a scaling factor, and the lattice constants, a_i, the remaining terms can be determined from optical measurements. Values of ΔH_{AB}, calculated by Phillips, are compared to ΔH_{AB} values measured by calorimetry in Table 3.2. Calculated values are within 10% of the measured values.

Considering for example the compounds found in a SiC-reinforced aluminum matrix composite (i.e. SiC and Al_4C_3), and using Phillips experimental spectroscopic data for SiC and Eqn. 3.3 above, the ΔH's for SiC and Al_4C_3 were calculated and presented in Table 3.2. The isotoropic band gap Eg for Al_4C_3 from these calculations is 8.4 eV. Measured values are also presented in Table 3.2 for comparison.

The form of Phillips equation is significant since covalent, metallic, and ionic type bonding contributions are all included; and all types of bonding contribute to the observed electronic transitions. This approach links together the possible fundamental bonding types that occur at interfaces to experimentally measurable parameters; i.e. the correlation between measurable optical transition energies to cohesive and formation energies. Hence, any condensed matter, regardless of relative contributions from each bonding types, should manifest a good correlation between optical transition energies and cohesive energy. It is this approach which spirited the development of a surface free energy model/expression for metallic materials which is subsequently presented in the next section.

TABLE 3.2 - Enthalpies of Formation (Kcal/mole)

Crystal	$-\Delta H$(Phillips)	$-\Delta H$(exp)
ZnSe	39.8	39.0
InSb	9.0	7.3
GaP	24.8	24.4
SiC	24.7	17.1*
Al_1C_3	~52.2	51.5*

*NOTE: Ref., JANAF TABLE

3.2 Surface Energy Relation for Metals

Although Phillips' approach was developed for Group IV ceramic compounds which are partially ionic and partially covalent, the model does not work for compounds with only metallic bonds. Since there appeared to be no direct correlation between measurable electronic transition energies and the cohesive energy in metals, such an empirical correlation was developed as part of this study.

The origin of observable valence electron transitions in the absorption spectra of metals can vary, depending on whether the metal is an alkali, polyvalent, transition, or noble metal. In transition metals for example, measurable electronic transitions occur from the upper d-level to the Fermi level and from the lower d-level to the Fermi level. Friedel (3) has correlated d-band broadening (i.e. width) effects to the cohesive energy in a transition metal. Knowing upper and lower d-levels with respect to a reference energy level, the band width can be calculated and related to the cohesive energy in a transition metal.

In some metals, such as aluminum or magnesium, which are polyvalent, there are no d-bands and the valence electronic structure is characterized as nearly free electron bands, weakly perturbed by Bragg reflection planes. The interaction of the Fermi sphere with Bragg reflection planes results in characteristic electronic transitions between 'parallel bands'. This parallel-band effect, which is structural, along with the kinetic, free-electron like effect, are the essence of the cohesive energy expression for polyvalent metals.

In a less ordered state, such as a liquid, Papazian (4) was able to relate the surface tension of molten metals to the plasma frequency. In this state, the electronic structure could be considered as free electrons having a collective characteristic frequency (the plasma frequency)

and the magnitude of the plasma frequency was shown to predict the
cohesive energy of the material. A solid, however, is more ordered, and
an additional term is needed to account for the electronic structure. For
polyvalent metals, this 'parallel-band' transition energy, V_2, is
considered.

The following equation for polyvalent metals is therefore proposed:

$$\gamma^{s,o} = C_1 (h\omega_p)^{1/2} (V_2)^{1/2} n^{2/3} \qquad (3.4)$$

In Eqn. 3.4, ω_p is a characteristic electron frequency that is
determined optically from the dielectric function; for nearly free
electrons, this frequency is equal to the plasma frequency. V_2 is a
'parallel-band' transition energy. The electron density, n, appears as a
result of the surface area of the Fermi sphere. The values for V_2 are
from the predicted parallel-band absorption edges of Harrison (5). In
nearly every case, the strongest predicted edge is used in the calculation
of $\gamma^{s,o}$. Since there are limited optical absorption measurements on
polyvalent metals, Harrison's predicted transition energies for V_2 were
the only consistent set of values available. For some metals, such as
aluminum, the predicted absorption edges are within 5% of the measured
values.

A plot of $(h\omega_p)^{1/2}(V_2)^{1/2}n^{2/3}$ versus $\gamma^{s,o}$ (measured surface tensions
at 0°K (6)) for polyvalent metals is shown in Fig. 3.1. To extend
this model to other metal types, copper was included as an example.
Copper is a noble metal with filled d-shell and no parallel band
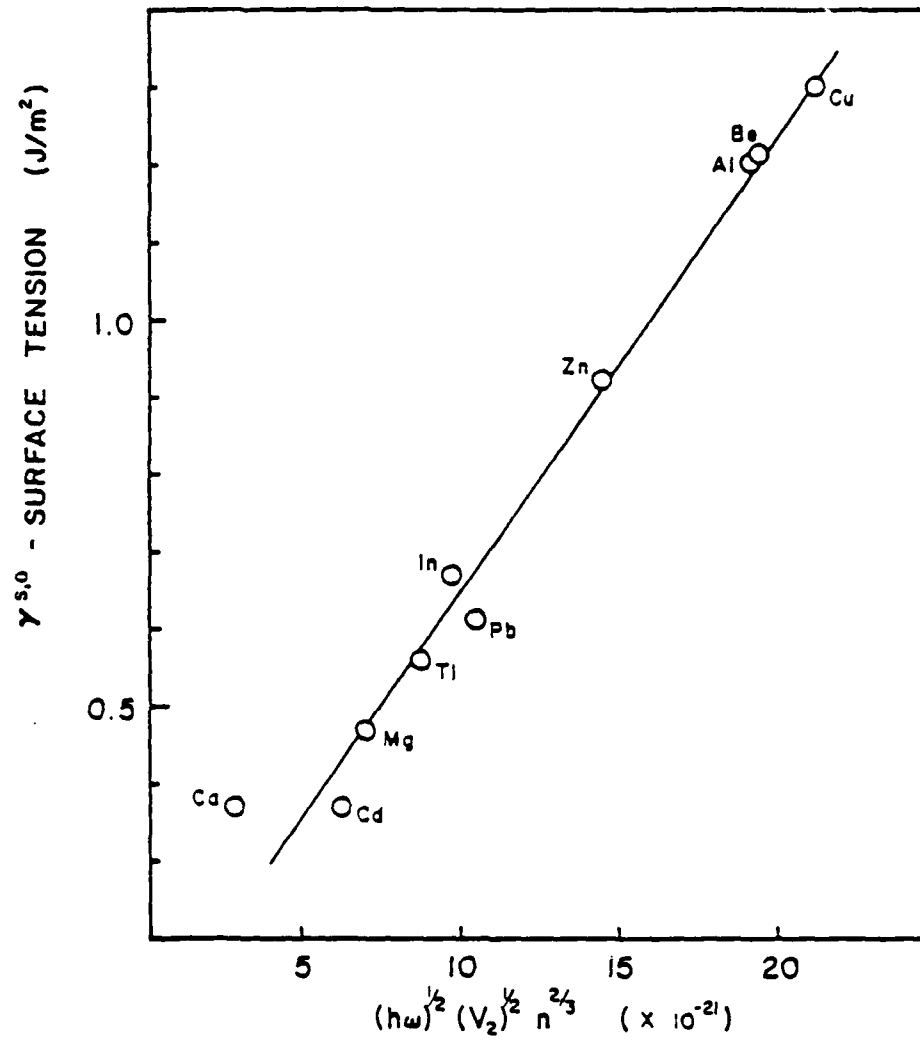transitions. Yet, the transition from the upper d-level to the Fermi

Figure 3.1   Correlation between the surface energy and the emphirical relation for pure metals

level seems to fit well in the proposed correlation. This is not surprising when considering Friedel's correlation for transition metals with unfilled d-shells. In the copper case, the position of the upper d-band, rather than the width of the d-band, appears more appropriate.

3.3 Experimentation

For ceramic materials, standard optical absorption measurements are used to determine direct interband transitions in the valence band. However, in metals, the absorption from free electrons mask the absorption/oscillations from 'bound' electrons in the optical spectra. Conventional spectral reflectance measurements of metals lack sharp structure due to the spreading of energy levels into energy bands. Using differential optical reflectance, or modulation spectroscopy in this case, critical interband transitions (due to 'bound' electrons) are resolved in an otherwise featureless spectra. The derivative of the unperturbed reflectance spectra is measured with respect to an external parameter, such as electric field, incident photon wavelength, or sample composition.

For this investigation, the proposed surface free energy expression for metals was verified using differential optical reflectance. Sample composition was used as the external parameter to modulate the electronic structure.

To illustrate the concept of composition modulation, a schematic band structure of copper, showing the effect of solute addition, is given in Fig. 3.2. The structure is centered at the L-symmetry point (111). This schematic shows the change in band energy for different crystallographic directions in reciprocal space. The solid and dashed lines refer to a pure copper and a dilute copper-based alloy respectively.
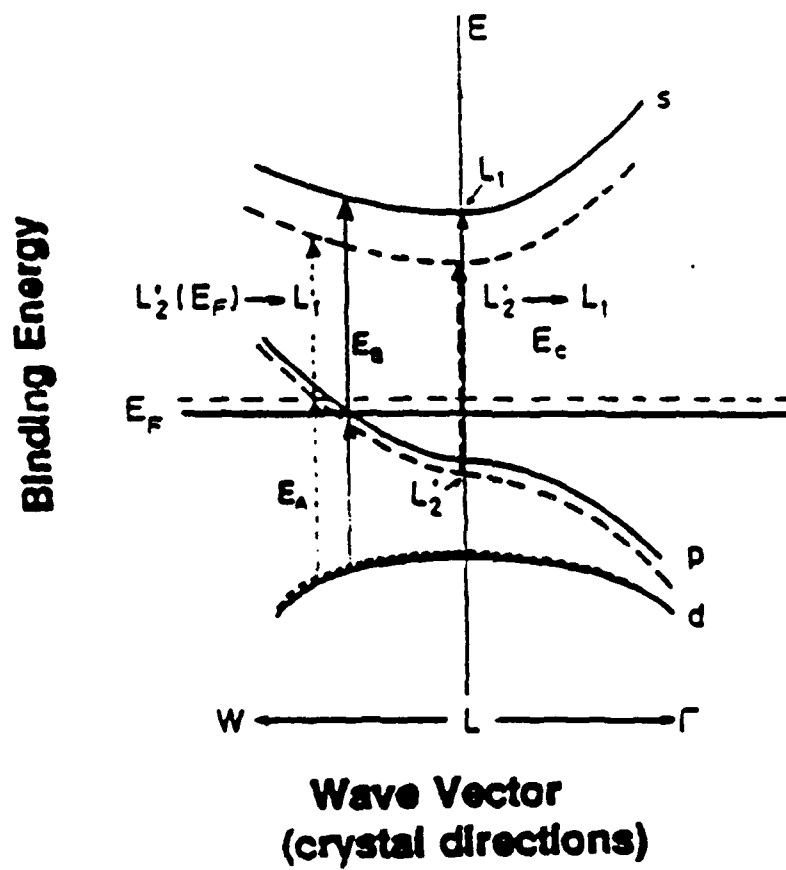
Figure 3.2   Schematic bond structure near L for copper and an assumed
copper based alloy.

In a composition modulation spectrum, the lattice periodicity is retained, the optical transitions remain vertical, and interband transition energy changes with the perturbation (i.e. E_A and E_B in schematic). Any change in the energy, within a hundredth of an electron volt, results in a large peak in the differential spectrum. These characteristic transitions, which occur at 'critical' points in the band structure, relate to the surface energy relation (4). As a means for comparison and calibration with similar reflectance work (7), copper-zinc alloys were used in this study.

A schematic of a typical differential reflectance apparatus is shown in Fig. 3.3. The fiber optic bundles are not typical, but rather a special modification for these tests. Unpolarized, monochromatic light from the source strikes the samples at near normal incidence. The reflected light is electronically processed to yield $\Delta R/R = 2(R_1 - R_2)/(R_1 + R_2)$. Owing to the nature of the differential reflectance technique, the effects of instrument parameters, such as background noise, or intensity fluctuations, are effectively eliminated.

For this experimentation, the optical configuration of a Carey 14 Spectrophotometer was modified to process reflective signals. To reflect light to and from the samples, fiber optic bundles were inserted into the light path at the point where it enters the photocell. The analog output of the Carey 14 is the ratio of the transmitted or reflected intensities between the sample and reference beams. In terms of differential reflectivity, the output transmission, T, from the Carey 14 is equal to $1 - \Delta R/R$.
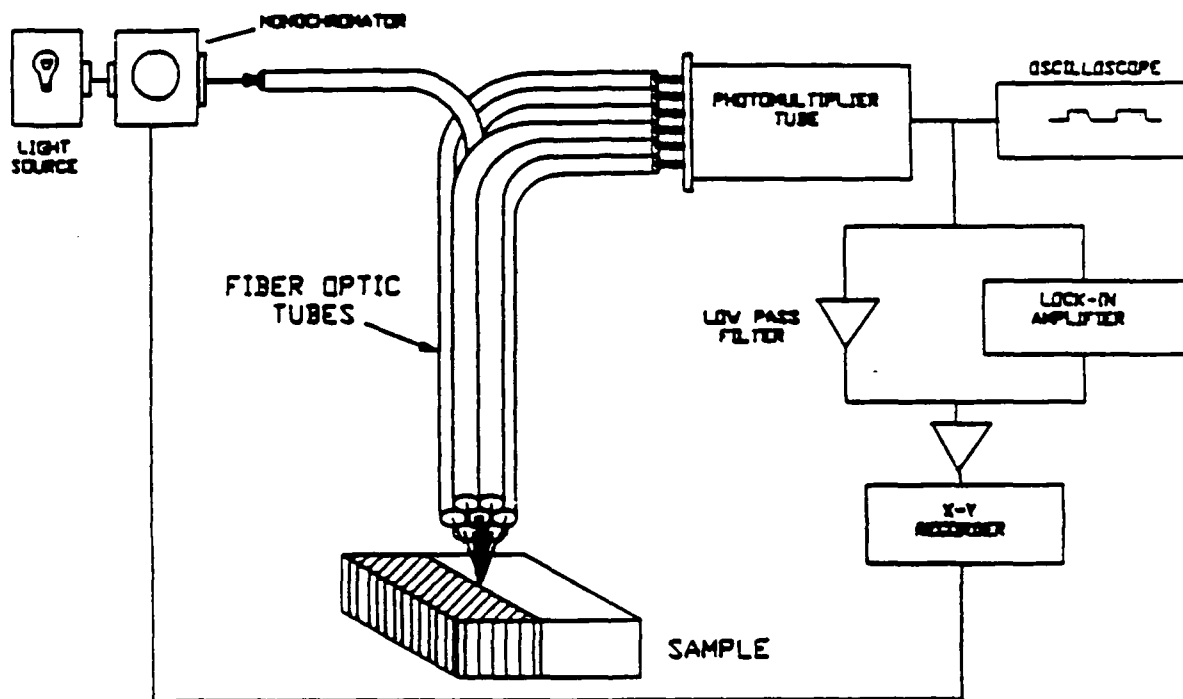
Figure 3.3   Schematic diagram of differential spectrometer.

To resolve features in copper's electronic structure, solute composition variations should be no more than 1-2%. The observed modulation spectrum is for the average zinc concentration between the reference and sample compositions. For these preliminary tests, however, the compositional variation between samples was sometimes more than 2% even though the mean value is reported.

3.4 Discussion of Differential Reflectance Measurements

Results from the reflectance measurements for copper-zinc alloys are shown in Fig. 3.4. The horizontal dashed line is the differential reflectance response between identical specimens. This line essentially represents the absorption characteristics of the acrylic fibers. For each set of samples, a reflectance spectrum was measured with the low zinc sample placed in the reference beam. Another spectrum was then measured with the high zinc sample placed in the reference beam. The absorption peaks are more easily discerned when these 'positive' and 'negative' spectra are superimposed.

The results indicate that, as the zinc concentration increases, the characteristic transition energy from the upper d-level to fermi level also increases (shown by the vertical dashed line). Our results are within 0.03 eV of the reported results from Hummel et al (7).

Having measured the transition energy, V_2, and determined the surface energy from Eqn. 3.4, the interfacial bond energies versus solute additio? for the copper/copper-zinc system were calculated (using Eqn. 3.1. These results, using data from this study, are shown as the dashed line in Fig. 3.5. Using transition energy data from Hummel et al (7),
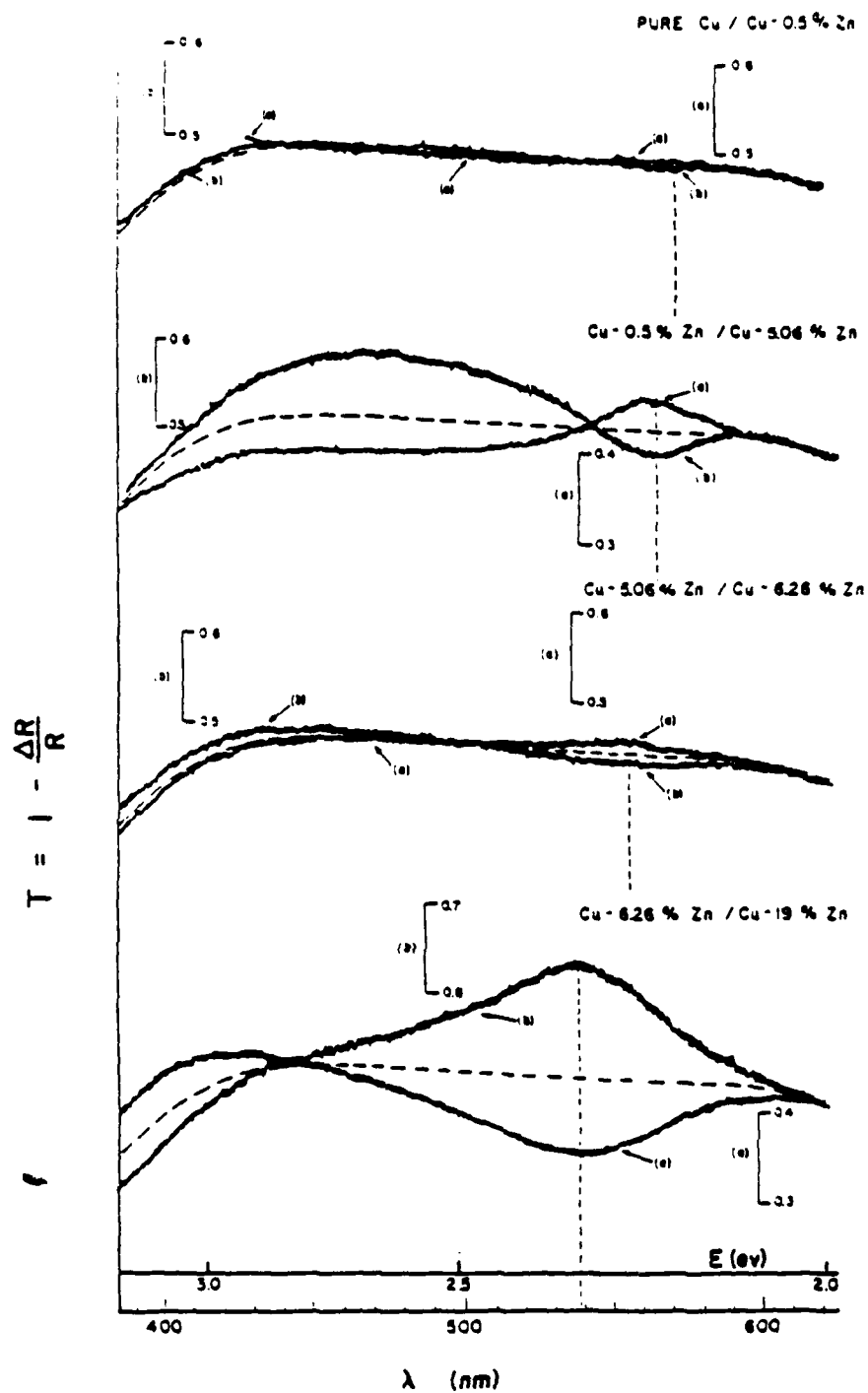
Figure 3.4   Experimental differential reflectogram for various
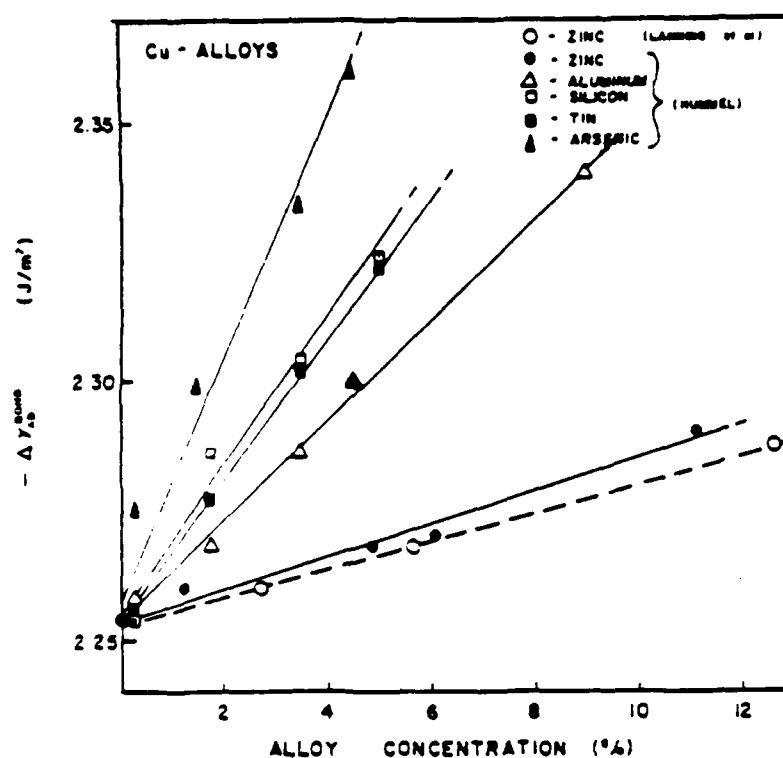copper-zinc alloys.

Figure 3.5   Calculated interfacial bond energies versus solute
concentrations for pure copper/copper systems.

interfacial bond energies for other copper/copper alloy systems were also calculated and plotted in Fig. 3.5.

Interfacial bond energies for metal/ceramic interfaces can readily be calculated using the methodology outlined above. For example, assuming a pure copper/SiC interface, and assuming negligible effects from the interaction parameter (i.e. γ^{ss}=0), the projected interfacial bond energy was calculated to be on the order of 3.0 J/m^2.

Although not measured in this study, the optical transitions for aluminum/aluminum alloys could be measured with differential reflectometry and used to calculate surface energies according to Eqn. 3.4. Transition energies for aluminum, aluminum-magnesium, and aluminum-lithium were determined by Benbow and Lynch (8) from low temperature (4°K) thermal conductivity measurements. It should be noted that thermal conductivity measurements in metals are limited to low temperatures. As the temperature increases, the strength of the free electron absorption increases and the characteristic transition energies cannot be determined. Using differential reflectometry, however, these transition energies can be resolved at room temperature. Nevertheless, surface energies were determined for aluminum and aluminum alloys from transition energy measurements.

The calculated interfacial bond energy (from Eqn. 3.1) for the pure aluminum/SiC system, assuming no carbide formation, is equal to 2.9 J/m^2. If aluminum carbide were to form between the aluminum matrix and the SiC reinforcement, then the interaction parameter, $\alpha\Delta H_f(Al_4C_3)$, is added onto the interfacial bond energy. The calculated interfacial bond energy for this case is equal to 3.07 J/m^2. These predicted bond

energies are ~50% greater than the predicted cohesive energy for pure Al-Al bonds.

The effect of alloy addition on the Al/SiC bond energy is shown in Fig. 3.6. This analysis only takes into account the chemical interaction between the substrates and there is no mechanical or diffusional contribution.

3.5 Conclusions

A method was developed in this study to correlate the characteristic transition energies in metals to the free surface energies of the solid. These surface energies were used in conjunction with the cohesive energy expression, developed by Phillips et al, for semiconductor (ceramic) materials to predict metal/metal and metal/ceramic bond energies.

A key aspect of this investigation was the incorporation of an optical technique, differential reflectometry, to measure the characteristic transition energies in the valence band structure of metals. Although standard optical absorption measurements are used to measure direct band gap transitions in semiconductors, the differential reflectance technique is used to enhance the 'critical' interband transitions in metals. The conceptual format of the above surface energy correlation for metals, along with the sensitivity of the Carey 14 Spectrophotometer adapted for these measurements, was validated with a copper/zinc alloy.

Using the predicted surface energies, based on optical parameters, and Miedema's bond energy relation, interfacial bond energies were presented for copper/copper alloys, aluminum/aluminum alloys, and the
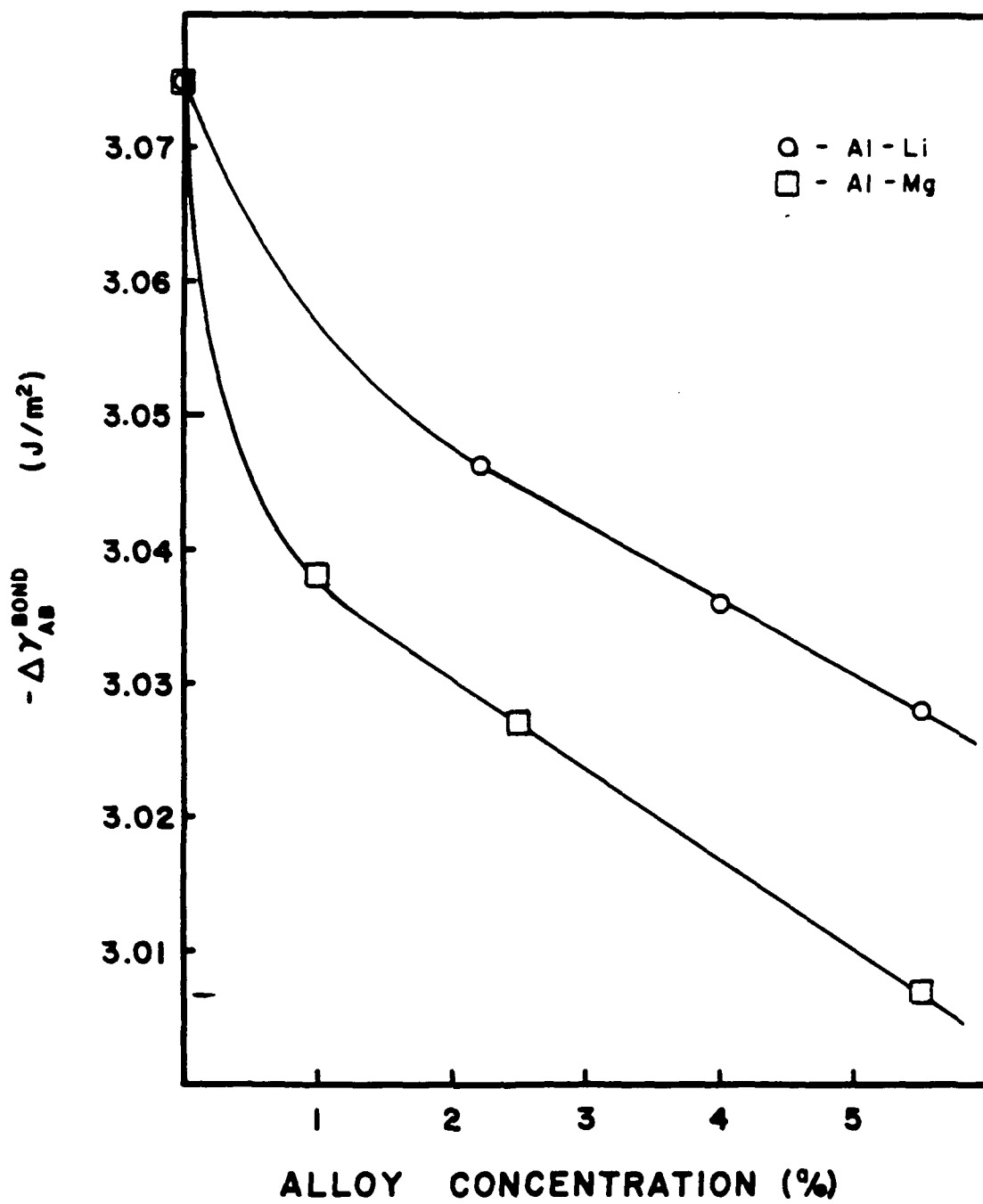
Figure 3.6   Interfacial bond energy as a function of solute concentration for aluminum/SiC system.

metal/SiC systems. These predicted interfacial energies are part of an ongoing effort to understand metal/ceramic interfacial bond strengths in terms of measurable electronic parameters.

3.6 References

1. Miedema, A.R., and den Broeder, J.A.; "On the Interfacial Energy in Solid-Liquid and Solid- Metal Combinations", Z. Metallkde., Vol. 70, No. 1, (1979), p. 14.

2. Phillips, J.C., and Van Vechten, J.A.; "Spectroscopic Analysis of Cohesive Energies and Heats of Formation of Tetrahedrally Coordinated Semiconductors", Phys. Rev. B, Vol. 2, No. 6, (1970), p. 2147.

3. Friedel, J.D., "Electronic Structure of Primary Solid Solutions in Metals", Advances in Phys., Vol. 3, (1954), p. 446.

4. Papazian, H.A., "Plasma Frequency Correlation of Liquid Metal Surface Tensions", High Temperature Science, vol. 18, (1984), p. 19.

5. Harrison, W.A, "Parallel-Band Effects in Interband Optical Absorption", Phys. Rev., vol. 147, no. 2, 1966, pp. 307.

6. Tyson, W.R., "Surface Energies of Solid Metals", Canadian Metallurgical Quarterly, vol. 14, no. 4, (1975), pp. 307.

7.   Nastasi-Andrews, R.J., and Hummel R.E.; "Optical Properties and
     Electronic Structure of Dilute Cu-Au, Cu-Zn, Cu-Al, Cu-Ga, Cu-Si,
     Cu-Ge, Cu-Sn, and Cu-As Alloys", Phys. Rev. B, Vol. 16, No. 10,
     (1977), p. 4314.

8.   Benbow, R.L., and Lynch, D.W.; "Optical Absorption in Al and Dilute
     Alloys of Mg and Li in Al at 4.2 K", Phys. Rev. B, Vol. 12, No. 12,
     (1975), p. 5615.

4.0 FUTURE WORK

Research will continue to emphasize better ways to evaluate interfacial bond strength and to characterize and optimize the infiltration kinetics of metal matrix composites.

4.1 Infiltration Kinetics

Further study of the incubation phenomenon is in progress. Emphasis will be placed on alloying effects, especially concentrating on additions of magnesium and silicon to pure aluminum. Preliminary feasibility tests are in progress investigating unique ways to infiltrate graphite by magnesium. Further studies are investigating new methods of applying a force to the metal infiltrant so as to more readily overcome the incubation resistance.

4.2 Wettability Studies

Research will continue to refine the accuracy with which wetting tendencies can be calculated from first principles. These calculations will be substantiated by experimental capillary rise measurements as described in Section 2.0.

4.3 Predictions of Interfacial Properties

Research in electronic bond strength prediction is expected to continue in the following three areas:

1. Differential optical reflectance studies of metals and alloys.

2. Optical absorption characterization of ceramic substrates.

3. Optical reflectance measurements of Al/SiC interfaces. Since SiC is transparent to electromagnetic radiation in the visible frequency, the surface state modifications in aluminum can be measured directly by transmitting the beam through a thin SiC layer.

5.0 ACKNOWLEDGMENTS